ORNL/SPR-2025/3806
M2LW-25OR0407023

## Light Water Reactor Sustainability Program

# Literature Review of Potential Synergistic Degradation Modes in Reinforced Nuclear Concrete

Yann Le Pape

March 2025

U.S. Department of Energy
Office of Nuclear Energy

ORNL/SPR-2025/3806
M2LW-25OR0407023

# Literature Review of Potential Synergistic Degradation Modes in Reinforced Nuclear Concrete

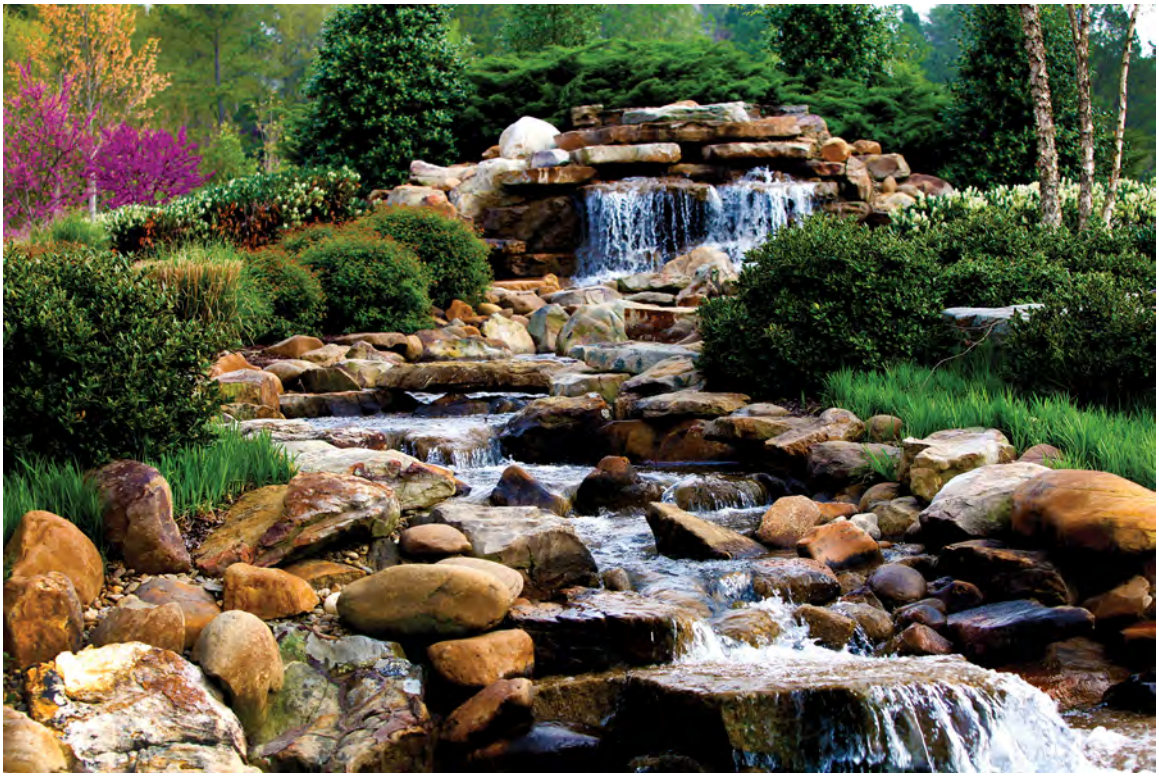

**Approved for public release.**
**Distribution is unlimited.**

Yann Le Pape[1]

**March 31, 2025**

[1]Oak Ridge National Laboratory

OAK RIDGE National Laboratory

ORNL IS MANAGED BY UT–BATTELLE LLC FOR THE US DEPARTMENT OF ENERGY

**ORNL/SPR-2025/3806**
**M2LW-25OR0407023**

Nuclear Energy and Fuel Cycle Division

# LITERATURE REVIEW OF POTENTIAL SYNERGISTIC DEGRADATION MODES IN REINFORCED NUCLEAR CONCRETE

Yann Le Pape[1]

March 31, 2025

Prepared by
OAK RIDGE NATIONAL LABORATORY
Oak Ridge, TN 37831
managed by
UT-BATTELLE LLC
for the
US DEPARTMENT OF ENERGY
under contract DE-AC05-00OR22725

## CONTENTS

## LIST OF FIGURES

## LIST OF TABLES

## LIST OF ABBREVIATIONS

| | |
|---|---|
| **AAR** | alkali-aggregate reaction |
| **ACES** | towards improved Assessment of safety performance for long-term operation of nuclear Civil Engineering Structures |
| **ASR** | alkali–silica reaction |
| **BSF** | blast furnace slag |
| **BWR** | boiling water reactor |
| **C-S-H** | calcium silicate hydrates |
| **CBS** | concrete biological shield |
| **CCB** | concrete containment building |
| **CVR** | centrum výskomu ŘeŽ |
| **DOE** | US Department of Energy |
| **dpa** | displacement per atom |
| **EIS** | electrochemical impedance spectroscopy |
| **EMDA** | Expanded Materials Degradation Analysis |
| **EPRI** | Electric Power Research Institute |
| **EU** | European Union |
| **FA** | fly ash |
| **FEM** | finite element model |
| **FTIR** | Fourier-transform infrared spectroscopy |
| **GB** | grain boundary |
| **GBs** | grain boundaries |
| **HCP** | hardened cement paste |
| **IAASR** | irradiation-assisted alkali-silica reaction |
| **IAC** | irradiation-assisted corrosion |
| **IASCC** | irradiation-assisted stress-corrosion cracking |
| **ICIC** | International Committee on Irradiated Concrete |
| **IEA** | ionization-enhanced annealing |
| **IRSN** | Institut de Radioprotection et Sureté Nucleaire |
| **JCAMP** | Japan Concrete Aging Management Program |
| **LCOE** | levelized cost of electricity |
| **LOCA** | loss of coolant accident |
| **LTO** | long-term operation |
| **LWR** | light-water reactor |
| **LWRS** | Light Water Reactor Sustainability |
| **MCNP** | Monte Carlo N-particle |
| **MD** | molecular dynamics |
| **MIBL** | Michigan Ion Beam Laboratory |
| **MIP** | mercury intrusion porosimetry |
| **NEUP** | Nuclear Energy University Program |
| **NIST** | National Institute of Standards and Technology |
| **NPP** | nuclear power plant |
| **NRC** | US Nuclear Regulatory Commission |
| **NSSS** | nuclear steam supply system |

| | |
|---|---|
| **OBE** | Operation Beyond Eighty |
| **OPC** | ordinary Portland cement |
| **ORNL** | Oak Ridge National Laboratory |
| **PDF** | probability distribution function |
| **PWR** | pressurized water reactor |
| **RBS** | Rutherford backscattering spectrometry |
| **RBSM** | rigid-body spring model |
| **RH** | relative humidity |
| **RIVE** | radiation-induced volumetric expansion |
| **RPV** | reactor pressure vessel |
| **SAD** | selected area diffraction |
| **SEM** | scanning electron microscopy |
| **SF** | silica fume |
| **SFHB** | spent-fuel handling building |
| **SONGS** | San Onofre Nuclear Generating Station |
| **SRIM** | Stopping and Range of Ions in Matter |
| **TEM** | transmission electron microscopy |
| **UCLA** | University of California at Los Angeles |
| **USD** | US dollars |
| **UTK** | University of Tennessee Knoxville |
| **VSI** | vertical scanning interferometry |
| **VVER** | water-water energetic reactor |
| **WKB** | Wentzel–Kramers–Brillouin |
| **XRD** | X-ray diffraction |

## EXECUTIVE SUMMARY

### Objectives

The Light Water Reactor Sustainability (LWRS) Material Research Pathway supports the long-term operation of light-water reactors (LWRs) by providing important data and methods to assess how systems, structures, and components in nuclear power plants perform and how damage can be reduced to ensure safe, economically sustainable operations. Over the last decade, research on concrete aging conducted by this program has been guided by findings from the Expanded Materials Degradation Analysis (EMDA), a joint effort involving the US Department of Energy (DOE), the US Nuclear Regulatory Commission (NRC), the nuclear industry, and academic institutions. One key conclusion from the EMDA regarding concrete structures is that

> *Irradiation of containment concrete is the most significant degradation mechanism, mainly due to the lack of data needed to fully understand how irradiation affects concrete's mechanical properties. Other factors, like alkali-aggregate reaction (AAR), acid attack, and creep, were found to be secondary. The biggest surprise was that susceptibility to fracture was ranked as the least important, which applies mainly to the type of concrete cracking typically considered in structural design. However, special forms of concrete damage could lead to the occurrence of fractures under specific conditions, such as when changes in structure or loading affect how cracks interact with creep. These specific cases are not considered general aging mechanisms and are dealt with separately.*

The LWRS program has contributed significantly to the understanding, characterization, and modeling of irradiation effects on concrete and its materials. Evidence of the program's impact is demonstrated by its many publications and the associated development of advanced methods and simulation tools. More than ten years after publication of the EMDA report, the expert panel's evaluations—based on their understanding, knowledge, and confidence—could benefit from a revision. It is likely that the updated findings on irradiated concrete would demonstrate increased confidence.

Remaining knowledge gaps in this field are discussed in this report. Although the EMDA report covers many degradation mechanisms affecting different types of concrete in LWRs, it mostly focuses on individual mechanisms. The present report aims to review and highlight some potential combined effects that may have been overlooked in the initial report in preparation for ongoing operations.

Understanding and assessment of the impact of irradiation on the performance of LWR containment structures, including the concrete biological shield (CBS), remain a priority. Two synergistic mechanisms associated with irradiation in the CBS are corrosion and alkali–silica reaction (ASR). This report also addresses how corrosion and ASR may interact, especially in nuclear structures exposed to environmental conditions like underground water contaminated with deicing chemicals.

### Key Conclusions from the Literature Review

#### Irradiation

A major gap in the data stems from the lack of understanding about how fast neutron flux rates affect concrete aggregate degradation. Early data from examining aggregate specimens exposed to radiation suggest a healing mechanism that depends on irradiation temperature, but further research is needed to fully understand how this works and how it can be applied to real-world conditions in LWRs. It is crucial to gather more data from actual in-service irradiated concrete specimens to make real progress in this area. Another data gap is

related to the effect of neutron irradiation on stress relaxation in concrete's cement paste, which was first documented in the 1970s. Although some theories exist, more experimental evidence is needed for a more definitive understanding of this issue. Understanding both of these mechanisms is expected to help improve the long-term operation of LWRs.

**Irradiation-Enhanced Alkali-Silica Reaction (IAASR)**
This issue mainly affects CBSs that have a metallic liner on the concrete surface facing the reactor cavity and concrete that maintains a high moisture content. Research from Japan, Europe, and the United States has documented how irradiation enhances the dissolution of aggregate minerals. However, the subsequent stages of the reaction, which lead to formation of expansive gel and concrete damage, are not well understood under irradiation conditions. More research is needed, including experimental irradiation studies, to better understand these mechanisms.

**Irradiation-Assisted Corrosion (IAC)**
Research in this area is limited, but it may involve both aerobic corrosion (in unlined CBSs) and anaerobic corrosion (in lined CBSs). Aerobic corrosion is linked to irradiation-induced carbonation of the concrete cover. Several knowledge gaps have been identified in this area, including (1) the role of gamma-ray dose rates in forming radiolytic gas and possibly accelerating drying, which affects the corrosion rate, (2) the role of temperature in corrosion rates during irradiation, and (3) the effect of fast neutrons on the formation of defects in the protective oxide layer and on reinforcement. New experimental designs are needed to address these gaps.

## ACKNOWLEDGMENTS

This research was sponsored by the US Department of Energy (DOE) Office of Nuclear Energy Light Water Reactor Sustainability (LWRS) program Materials Research Pathway under contract DE-AC05-00OR22725 with UT-Battelle LLC/Oak Ridge National Laboratory (ORNL).

# 1. INTRODUCTION

With the prospective increase in energy demand estimated to range from 30% to 76% through 2050 (US Energy Information Administration, International Energy Outlook 2023, https://www.eia.gov/outlooks/ieo/narrative/index.php), nuclear energy is expected to contribute to safe, reliable, economically viable electricity production to satisfy the nation's demand. To meet that objective, both newly built advanced nuclear reactors and extended operation of existing light-water reactors (LWRs) will be needed. An analysis of the levelized cost of electricity (LCOE) by generation technology concludes that the most competitive option is long-term operation (LTO) of LWRs, with an estimated cost of US dollars (USD) 25–50 USD/MWh (OECD/NEA No. 7524, 2021). Nuclear generation also benefits from the highest load factor across all generation plants (power availability 84% in 2020, European Energy and Transport – Trends to 2030, Update 2007, COM). Nevertheless, the March 2011 Fukushima Daiichi accident, rated as level 7 on the International Nuclear and Radiological Event Scale, dramatically increased societal demand for enhanced safety. Hence, although licensing extension of commercial nuclear power plants (NPPs) is economically viable, operation requires addressing the effects of the aging materials on the integrity, structural performance, and safety of the major NPP components, including the concrete biological shield (CBS), which provides radioprotection for personnel and equipment, along with structural support for the reactor pressure vessel (RPV) and the nuclear steam supply system (NSSS); the concrete containment building (CCB), which houses the nuclear reactor, its pressurizer, reactor coolant pumps, steam generators, and other equipment or piping that might otherwise release fission products to the atmosphere in the event of an accident; the spent-fuel handling building (SFHB); and the cooling water intake structure, among the most critical.

Each of these structures is subject to diverse in-service conditions associated with local atmospheric factors such as relative humidity (RH) and temperature, the presence of aggressive chemicals including chloride and sulfate, ingress of underground water, and exposure to irradiation and high temperature, to name a few.

In an effort to categorize the significance of various aging mechanisms, identify knowledge gaps, and prioritize research needs, a joint effort between industry, academia, the US Nuclear Regulatory Commission (NRC), and the US Department of Energy (DOE) led to the publication of the Expanded Materials Degradation Analysis (EMDA) report series, including one report specifically dedicated to nuclear concrete (Graves et al. 2014). The EMDA provides a thorough description of identified degradation modes for plain, reinforced, and pre-stressed concrete structures. However, the state of knowledge in this area has evolved over the past decade particularly regarding the effects of irradiation on concrete, which has been the subject of sustained research efforts domestically by the DOE Light Water Reactor Sustainability (LWRS) Program, NRC research activities, the Electric Power Research Institute (EPRI) LTO program, and internationally, the Japan Concrete Aging Management Program (JCAMP) and the European Union (EU) project "towards improved Assessment of safety performance for long-term operation of nuclear Civil Engineering Structures (ACES)". In addition, the EMDA considered degradation modes mostly independently, without thoroughly exploring the possible synergistic effects between them.

In anticipation of future license applications for reactor operation from eighty to one hundred years, or *Operation Beyond Eighty (OBE)*, research is needed to identify current gaps of knowledge. This report does not aim to replace the extensive effort comparable to the EMDA, but rather, it provides an update on the current state of knowledge regarding irradiation, alkali–silica reaction (ASR), and corrosion, along with an analysis of the synergistic effects of these mechanisms considered in pairs with irradiation, to identify potential knowledge gaps requiring future research. These synergistic modes are referred to as irradiation-assisted alkali-silica reaction (IAASR) and irradiation-assisted corrosion (IAC) in the present report.

## 2. INDIVIDUAL DEGRADATION MODES

### 2.1 IRRADIATION

#### 2.1.1 Exposure

In LWRs, the component most exposed to irradiation is the CBS, the function of which is to shield personnel and equipment from neutron bombardment and gamma rays exiting the RPV. The neutron flux and gamma dose rate at the surface of the concrete vary according to reactor design, the number of loops for the primary coolant system, and the designs of the core and the internals (e.g., hafnium absorber), as well as the presence or absence of a neutron shield tank.

Neutron kinetic energy varies, ranging from a low energy of a few meV (*cold*neutrons) to a very high energy above $\sim$ 1 MeV (*fast* neutrons). Based on Monte Carlo simulations, it is estimated that "95% of the displacement per atom (dpa) is generated (in minerals commonly found in concrete) by neutrons with energies above 0.1 MeV in pressurized water reactors (PWRs)"(and close to 100% of dpa for neutron energies above $E > 10$ keV) (Remec et al. 2018). The adopted energy threshold for rock-forming minerals is generally 0.1 MeV, although it is common to use $E > 10$ keV (Denisov, Dubrovskii, and Solovyov 2012).

At 80 effective years of operation, estimates of the maximum fast[1] neutron fluence at the surface of the CBS in PWRs at mid-core elevation ranging between $10^{19}$ n.cm$^{-2}$ and $6 \times 10^{19}$ n.cm$^{-2}$ at energies higher than 0.1 MeV (Esselman and Bruck 2013). The fast neutron flux is generally higher in three-loop PWRs and in Westinghouse and Combustion Engineering two-loop designs.

The fast neutron flux in boiling water reactors (BWRs) CBSs at 80 years of operation is an order of magnitude lower than in PWRs with an estimated maximum value of $\lesssim 3 \times 10^{18}$ n.cm$^{-2}$ at the surface of the concrete.

The gamma ray dose rate in operating PWRs ranges from approximately 20 to 30 kGy h$^{-1}$, which would result in a dose of about 175 to 250 MGy over 100 years of operation. There is no recent evidence of a gamma irradiation threshold above which concrete undergoes degradation.

Gamma heating is approximately 0.02 W g$^{-1}$. The corresponding temperature increase from other heat transfer mechanisms in the cavity does not appear to exceed the design limit of 150°F.

#### 2.1.2 Mechanisms

To date, available data on in-service irradiated concrete are limited. Data obtained from cores extracted from test reactors (e.g., the Oak Ridge National LaboratoryOak Ridge National Laboratory (ORNL) graphite reactor shield (Blosser et al. 1958)) have limited value because the fluence level is several orders of magnitude lower than the accepted threshold of $10^{19}$ n.cm$^{-2}$. Hence, the current understanding of the effects of irradiation on concrete and its constituents is primarily based on data obtained under accelerated conditions in test reactors.

**Neutron-induced damage in rock-forming minerals**

The primary degradation mechanism caused by irradiation is the amorphization of rock-forming minerals. $\alpha$-quartz is the reference rock-forming mineral in the fields of fundamental and engineering sciences; consequently, literature on the effects of irradiation on quartz is abundant.

1. Fast neutrons generally refer to energies higher than 1 MeV. The term "fast neutron" is conventionally adopted for energies higher than 0.1 MeV because they correspond to damaging neutron in concrete constituents (Remec et al. 2018).

Collisions between high-energy neutrons such as $E > 10$ keV ((Denisov, Dubrovskii, and Solovyov 2012)) and highly crystalline rock-forming minerals (or poorly crystalline hardened cement paste (HCP)-forming hydrates, although the consequences in terms of gradual disordering are fundamentally different) result in knock-off atoms and the subsequent formation of complex damage cascades (secondary knock-offs), ultimately concluding through a nuclear stopping mechanism."The Si−O bond is the weakest structural component during the amorphization of silicates" (Eby, Ewing, and Birtcher 1992).

Neutron, electron, or ion irradiation of minerals causes the accumulation of damage cascades, resulting in the gradual disordering of the pristine crystalline structure. This process is known as *amorphization* or *metamictization*, particularly when describing a natural process caused by the endogenous presence of radioactive materials such as the $\alpha$-radiation–induced recoil observed in zircon (ZrSiO), pyrochlore, monazite ($CePO_4$), and uraninite ($UO_2$) (R.C. Ewing et al. 1987; R. Ewing et al. 1988). Evidence of amorphization can be observed through (1) the disappearance of crystal-induced sharp spectra and the formation of a halo in selected area diffraction (SAD) patterns under transmission electron microscopy (TEM) (Inui et al. 1990; Eby, Ewing, and Birtcher 1992; Pignatelli, Kumar, Field, et al. 2016), (2) reflectivity change (W. Primak 1976), (3) Fourier-transform infrared spectroscopy (FTIR) spectra shift toward lower wave numbers and peak intensity decrease (Abdukadyrova 2008; Pignatelli, Kumar, Field, et al. 2016), (4) Rutherford backscattering spectrometry (RBS)/C channeling experiment (Manzano-Santamaría et al. 2012), (5) optical refractive index with the Wentzel–Kramers–Brillouin (WKB) method (Manzano-Santamaría et al. 2012), (6) Raman spectroscopy (Zubov and Osipova, 1971; Abdukadyrova 2004; Silva, Rosseel, and Kirkegaard 2018), and (7) X-ray diffraction (XRD)-based change of lattice parameter (Krivokoneva and Sidorenko 1971; Krivokoneva 1976; Seeberger and Hilsdorf 1982; Silva, Rosseel, and Kirkegaard 2018). Amorphization affects the chemical, physical, and mechanical properties of irradiated minerals.

**Gamma-induced damage in cementitious materials**

Gamma ray exposure in the CBS is mainly caused by rays exiting the RPV. However, secondary gamma rays are also produced from neutron irradiation of metal-bearing constituents, including low carbon steel reinforcement and heavy aggregates such as magnetite ($Fe^{2+}Fe_2^{3+}O_4$), hematite ($Fe_2O_3$), ilmenite ($FeTiO_3$), and barite ($BaSO_4$) used for shielding application. In the US reactor fleet, heavy aggregate usage is limited to a few BWR CBSs. Risner, Alpan, and Yang (2020) implemented an irradiation transport simulation of a prototypical PWR CBS and found that

> *the primary radiation damage impact resulting from rebar in concrete is production of capture gammas as thermal neutrons, which have been moderated and thermalized by scattering in the concrete, undergo radiative capture reactions in the steel. This absorption produces a range of capture gamma energies, which can be as high as* $\approx$ 8 MeV. *These capture gammas become the dominant contributor to the total heating rate and the gamma dose rate at a relatively short distance into the bioshield.*

The combined neutron and gamma heating in the reinforcement bar can reach 4–5 times the heating rate in the surrounding concrete.

Reactor gamma rays interact with concrete constituents primarily by Compton scattering (Kontani et al. 2013), which is the interaction and ejection of orbital electrons accompanied by a loss of energy. The primary effect of gamma in concrete is water radiolysis, which is the decomposition of water molecules due to ionizing radiation (Le Caër 2011). The energy levels of electrons ejected by Compton scattering are too low to affect the solid phase of cement paste and aggregates (Kontani et al. 2013).

The HCP formed from ordinary Portland cement (OPC) mixed with water mostly consists of a complex assemblage of poorly crystallized calcium silicate hydrates (C-S-H), Portlandite (calcium hydroxide), and an intricate, multiscaled network of pores partly filled with an ionic solution (Taylor and Newbury 1984).

The C-S-H structures are categorized between tobermorite- and jennite-like structures (Myers et al. 2013), or clay materials. Unlike heavy ions and neutrons, ionizing radiations ($\alpha, \beta, \gamma$) do not cause amorphization of clay minerals unless in high doses on the order of 1 GGy (kaolinite and smectites) (Allard 1994; Gournis et al. 2000, 2001; Allard and Calas 2009), suggesting a high tolerance of C-S-H against gamma irradiation.

Post-gamma-irradiation scanning electron microscopy (SEM) observations of mature HCP up to 1,409 MGy ($^{60}$Co irradiator operated at room temperature, activity of 1,036 TBq and dose rate of 38–40 kGy h$^{-1}$) "revealed the following steps of the damage process: decomposition of hydrates, separation of chemically bonded water causing the formation of air bubbles, appearance of pseudomorphoses and densification" (Łowińska-Kluge and Piszora 2008). Pure Portland HCP shows evidence of initial degradation at a dose of 130 MGy, whereas the introduction of pozzolanic phases in the form of silica fume (SF) and fly ash (FA) increased the irradiation resistance to approximately 290 MGy

Low-dose ($^{60}$Co source, less than 8 Gy h$^{-1}$, up to approximately 8 kGy) and moderate-dose ($^{137}$Cs source, < 2 kiloGy/h up to 32kGy) rate gamma irradiations were applied to mortar specimens made of OPC and blast furnace slag (BSF) cement, along with limestone sand and filler, at a very early age. This experiment was intended to simulate irradiation effects on waste disposal cementitious barriers (Craeye et al. 2015) and to study the interaction between irradiation and the formation of cementitious hydrates during the hydration phase. SEM analysis showed that needle-like ettringite ($C_3A_3 \cdot CaSO_4 \cdot 32H_{20}$) formed in the 5 kGy-irradiated mortar specimens made with BSF cement. Such a phenomenon was not observed in the specimens prepared with OPC. In all specimens, an increase of porosity correlated with strength reduction was observed. However, this was attributed to radiolytic gas release causing a loss of available free water for hydration-induced hardening.

**Radiolysis**

The formation of radiolytic gas in cementitious materials is complex because of interaction with elements present in the cementitious matrix and the alkaline pore solution.

After ~ 100 ns, ionization and, to a lesser degree, electronic excitation, cause the appearance of primary products of stable molecular or ionic nature ($H_2$, $H_2O_2$, $H^+$, $HO_2{}^-$: stable) or highly unstable free-radical nature ($e-_{aq}$, H, OH) (Bouniol and Aspart 1998). Notably, $O_2$ forms as a secondary product resulting from a set of complex chemistry reactions involving hydroxide ions. However, the disappearance of $O_2$ during water radiolysis in a cementitious environment has been reported by (Bibler and Orebaugh 1977; Bouniol and Aspart 1998), and radiolytic $O_2$ production appears to be exceptionally observed. The direct disappearance of $O_2$ is caused mainly by the attack of the $e-_{aq}$ radicals ($e-_{aq} + O_2 \longrightarrow H_2O + O_2\uparrow$ ) 2) and the $O^-$ radicals specific to the alkaline medium ($O^- + O_2 \longrightarrow O_3{}^-$). These reactions explain the rapid consumption of oxygen already present in unsaturated cementitious materials. However, in aqueous conditions, peroxides (primary radiolytic product) appear to react with calcium phases such as Portlandite: $Ca(OH)_2 + H_2O_2 + 6\,H_2O \longrightarrow CaO_2{\bullet}8\,H_2O_2\downarrow$. Peroxide octahydrate ($CaO_2{\bullet}8\,H_2O_2$) is "very slightly soluble, but capable of easily losing its water of crystallization in air and then decomposing with simultaneous carbonation." (Bouniol and Aspart 1998) Hence, it cannot be observed once the irradiation experiment ends. However, it can be inferred that such a *passing* mechanism involving peroxide octahydrate is likely the result of the formation of vaterite (hexagonal calcium carbonate) and aragonite (orthorhombic) instead of calcite (trigonal) under gamma irradiation as observed by Maruyama et al. (2018). More specifically, these authors found that the content of calcium carbonates measured in white OPC paste specimens irradiated at approximately 55 MGy (duration: ~250 days, temperature: ~ 23 ± 10 °C, and ~ 58% ± 20% RH) was 0.66 g g$^{-1}{}_{hcp}$ and 0.45 g g$^{-1}{}_{hcp}$, for specimens pre-equilibriated at 100% and 50% RH, respectively. The initial carbonated content was approximately 0.05 g g$^{-1}{}_{hcp}$. The carbonate contents of unirradiated specimens placed in comparable temperature and RH conditions were 0.65 g g$^{-1}{}_{hcp}$ and 0.55 g g$^{-1}{}_{hcp}$, for specimens

pre-equilibriated at 100% and 50% RH, respectively. Hence, the carbonate content was not significantly modified by irradiation during this experiment. However, the nature of the carbonates produced during irradiation was different: significant substitution (about 50%) of calcite by vaterite and aragonite was observed. This phenomenon is attributed to rapid drying of the HCP caused by gamma-ray heating and radiolysis of water, as well as precipitation of unstable peroxide octahydrates.

In contradiction with the results found in Maruyama et al. (2018), Dabrowski et al. (2022) observed an increase an the peak intensity of calcite after gamma irradiation measured by XRD-Rietveld analysis, and an decrease of the Portlandite peak intensity after gamma irradiation.[2] Potts and Leay (2021) observed that the calcite:vaterite ratio ranged between 0.65 and 1.2 in post-gamma irradiation[3] carbonated[4] fly ash blended OPC paste specimens[5] (OPC:FA, 3:2) whereas it ranged between 0.6 and 0.8 in post 60 °C-thermal treatment carbonated specimens. In control specimens at room temperature, the calcite:vaterite ratio remains between 0.3 and 0.4. Hence, Potts and Leay (2021) suggest that advanced thermal dehydration caused by irradiation or thermal treatment and K and Na substitutions in carbonates are partially responsible for the change in the calcium carbonate polymorph switch in FA-bearing cement.

### 2.1.3 Properties

#### Chemical properties of irradiated minerals

Post 400 keV-Ar ion-implanted silicates, quartz (Pignatelli, Kumar, Field, et al. 2016), albite (Hsiao et al. 2017), and almandine (Hsiao et al. 2018) show an increase in dissolution rates measured by vertical scanning interferometry (VSI) (an optical scanning profilometry technique for periodically monitoring the loss of height of post-irradiation-induced minerals in contact with a caustic solvent[6]) by factors of ≈100 to reach that of fused quartz, ≈10 and ≈2, respectively, quite independently of the caustic solvent's pH. Hence, increased reactivity of aggregates induced by irradiation could theoretically cause the first stage of IAASR formation (Ichikawa and Koizumi 2002; Ichikawa and Kimura 2007), or it could increase the reactivity of ASR-susceptible aggregates potentially used for radiation shielding concrete (Jóźwiak-Niedźwiedzka, Jaskulski, and Glinicki 2016). This question is discussed in detail in the section addressing possible synergies between irradiation and ASR.

#### Physical properties of irradiated minerals

Neutron irradiation causes rock-forming minerals to change the density of amplitude, varying with their composition, as well as their crystalline structure. For example, a large decrease of the density of irradiated $\alpha$-quartz, ≈ 15% (≈ 18% in volume expansion, was abundantly documented (Wittels and Sherrill 1954; Primak 1958; Mayer and Lecomte 1960), whereas vitreous silica exhibits a density increase or contraction, of about 2–3% (Primak 1958; Mayer and Lecomte 1960). In general, irradiated silicates exhibit a loss of density. Expansions of minerals do not occur isotropically along or perpendicular to the optical axis (Primak 1958; Denisov, Dubrovskii, and Solovyov 2012). The irradiated quartz density still decreases, whereas the system's enthalpy rapidly reaches a plateau (Krishnan et al. 2017). Isothermal expansion of irradiated $\alpha$ quartz follows a sigmoidal evolution with increasing dose (Primak 1958; Zubov and Ivanov 1966). At a given expansion, the lattice parameter measured by XRD seems to be independent of the irradiation temperature history (Bykov et al. 1981). However, the expansion rate decreases with increasing irradiation temperature because of point-defect annealing. Data on the effects of irradiation temperature on quartz were

2. The details of Dabrowski et al. (2022) are provided in section 3.2.

3. Dalton Cumbrian Facility's 60Co irradiator at 23 kGy $h^{-1}$ to reach a dose of about 1.5 MGy. Average irradiation temperature: 60 °C.

4. 10-h exposure in an atmosphere at 5% $CO_2$ content.

5. Cured for 6 weeks in lime saturated water at 20 °C.

6. Experimental protocol described in (Pignatelli, Kumar, Field, et al. 2016).

carefully collected (Bykov et al. 1981). Although the final volume expansion appears to be independent of the irradiation temperature, the expansion rate exhibits a rapid decrease with increasing temperatures in the range of ≈ 30 °C to 600 °C following an Arrhenian trend, which apparently corresponds to nucleation growth theory (Maruyama et al. 2017; Le Pape, Alsaid, and Giorla 2018). Because Bykov et al. (1981) observed that the irradiation temperature in the range of ≈ 30 °C to ≈ 300 °C significantly affects the radiation-induced volumetric expansion (RIVE) rate—the higher the irradiation temperature, the lower the rate—it can be hypothesized that this effect is governed by thermal annealing. However, the interpretation of published results from post-irradiation annealing experiments (Primak 1958; Yano et al. 2007) using a simple activation energy spectrum model proposed by Hickman and Pryor (1964) shows that thermal annealing is unlikely to be a dominant mechanism for defect healing during neutron irradiation at temperatures $\lessapprox$ 350 °C (Le Pape et al. 2024). The apparent effect of irradiation temperature on the RIVE rate must be interpreted differently. Higher irradiation temperatures imply greater undissipated heat resulting from radiation-induced energy deposition, notably from thermal neutrons and gamma rays. At this stage of the research, the hypothesis of ionization-enhanced annealing is proposed but requires further investigation.

**Mechanical properties of irradiated minerals**

Amorphization or gradual disorder formation causes the isotropization of the elastic tensor as observed on irradiated $\alpha$ quartz. The pristine crystal structure of $\alpha$-$SiO_2$ is a trigonal (rhombohedral) lattice system. This is characterized by 7 independent elastic constants. In particular, the compliance constant $s_{14}$ determined by resonant frequency analysis rapidly decreases with neutron irradiation until it vanishes completely (Mayer and Gigon 1956; Mayer and Lecomte 1960). However, other elastic constants do not necessarily evolve monotonically with increasing fluence (Zubov 1956; Mayer and Lecomte 1960; Zubov and Ivanov 1967), such as monotonic decrease ($s_{11}$), monotonic increase ($s_{33}$), non-monotonic ($s_{12}$), or vanishing ($s_{14} \to 0$), thus illustrating the complexity of the amorphization-induced *isotropization* of quartz. Interpretations of molecular dynamics (MD) simulations of various irradiated minerals (mostly silicates) have shown that the Young's modulus of an equivalent polycrystalline assemblage with randomly distributed orientations can be approximated by a cubic function of the density change (Krishnan et al. 2018).

**Mechanical properties of irradiated rocks**

Most CBSs in LWRs were built with natural aggregates obtained from local quarries to minimize transportation costs during construction. Because of the diversity of geological formations across the contiguous United States, there is significant variability in the nature and mineral content of the aggregates used. For illustration, it is known that San Onofre Nuclear Generating Station (SONGS) aggregate is made of metamorphic rock, including a variety of altered rocks with igneous (granite), volcanic, and sedimentary (shale) origins (Le Pape et al. 2022). Detailed information about each aggregate used for the construction of the 63 operational US PWRs is not available. However, the diverse geology of the United States suggests significant mineralogical variations.

In addition, rock-forming aggregates may have been subject to weathering, erosion, deposition, cementation in sedimentary rocks, or metamorphism at high temperatures and pressures, or they may have been subject to some combination of these factors. These conditions can cause mineral transformations and mineral structure deformations. Hence, rocks can be considered assemblages of more or less crystalline grains of minerals with pre-existing defects. The grain size distribution varies with the formation process. For example, intrusive magmatic rocks exhibit larger grain sizes than extrusive magmatic rocks as a result of different cooling rates. Each individual grain is subject to radiation-induced amorphization and expansion. Because radiation-induced expansion is not isotropic (i.e., it varies with the crystal axis) and different minerals exhibit different expansion rates and intensities (Denisov, Dubrovskii, and Solovyov 2012), incompatible strains develop either at the mineral grain boundary (Clark 1958) or within individual grains, causing the formation

of microcracks (Maruyama et al. 2023). The presence of quartz grains in silicated rocks appears to govern the cracking pattern in adjacent minerals (Maruyama et al. 2023). Cracking contributes to the expansion of irradiated rocks (Denisov, Dubrovskii, and Solovyov 2012; Le Pape, Sanahuja, and Alsaid 2020; Maruyama et al. 2023).

**Mechanical properties of irradiated concrete**

### 2.1.4 Structural Significance

**Irradiation, temperature, and moisture content**

The only concrete structure subject to high radiation in an LWR is the CBS. The main function of the CBS is to protect personnel and equipment against severe neutron flux and gamma dose rate. When natural aggregates are used, the attenuation of neutrons is mainly caused by the high cross-section of hydrogen present in the water at the time of concrete mixing (Kaplan 1983, 1989). Limited hydrogen content can be also found in some minerals such as phyllosilicates. The interaction between hydrogen and neutrons and the design of the fuel core in the reactor lead to nonuniform neutron flux in the CBS, which varies spatially with elevation, depth, and azimuth (Field, Remec, and Le Pape 2015; Cheniour et al. 2023). In addition, some designs do not include a metal liner at the inner surface of the CBS, which causes drying and thus affects the hydrogen content in the area most exposed to irradiation-induced damage.

The fast neutron flux is at its maximum at the elevation of the mid-fuel core. The profile of irradiation-induced damage depths shows a sharp change at approximately 1.5 m from the fuel core at mid-elevation. The evolution of the flux profile with height exhibits a sharp drop above and below approximately 1.5 m from the fuel core at mid-elevation based on irradiation transport simulations obtained using Monte Carlo N-particle (MCNP) (Remec 2013). Attenuation in the radial direction (depth of the CBS) depends on the hydrogen content and approximately follows an exponential law. The fast neutron flux ($E > 0.1$MeV) decreases by an order of magnitude over a depth of approximately $20 \pm 5$cm. This specific depth value is provided for illustration purposes, but it may vary from one reactor to another. The region subject to fast neutron fluence is spatially limited in the concrete facing the RPV.

In addition to the nonuniform neutron flux, the moisture content is expected to vary within the CBS because of drying at moderate temperature and water radiolysis. Even without radiation, mass concrete in LWRs exhibit important variations of moisture content after decades (Oxfall 2016). Although the concrete's strength and Young's modulus increase with age, important variations are observed across a thick wall (Yokokura et al. 2024; Uchikoshi, Koshiro, and Koyama 2024).

The temperature field also varies according to the design of the reactor vessel and piping, the geometry of the CBS, and the irradiation-induced energy deposition in the concrete.

Irradiation transport, heat transfer, and moisture transport in the concrete shield wall are coupled mechanisms (Le Pape 2015). To this date, CBS structural evaluations accounting for these fully coupled effects do not appear to have been published.

**Structural performance**

A review of published models addressing in-service structural performance of PWRs can be found in this report Le Pape, Alnaggar, and Cheniour (2023).

The first model addressing the structural effects of irradiation-induced volumetric expansion on the CBS was published by Andreev and Kapliy (2014). The technical merit of this 1D-radial analytical model in the elastic regime is to establish that the attenuating fluence profile leading to nonuniform RIVE causes formation of important compression stresses in the concrete shield wall near the reactor cavity. These stresses result

from the structural constraints imposed by the thickness of CBS in the vertical and orthoradial directions. These compression stresses are balanced by moderate tensile stresses toward the back of the CBS. A more comprehensive model, including the effects of irradiation on the mechanical properties of concrete (Field, Remec, and Le Pape 2015), was later published by Le Pape (2015). The probabilistic study included in this research concluded that approximately 6% of the CBS depth is subject to elastic stresses exceeding the strength of concrete. From the perspective of constitutive models, the main limitation of this model is the absence of mechanical damage. The excessive elastic energy can only be dissipated by cracking or stress relaxation.

More advanced models were developed to account for the formation of inelastic deformations using either a plasticity-based continuum finite element model (FEM) (Bruck et al. 2019) or quasi-brittle mesoscale models (Giorla, Le Pape, and Huang 2016) and rigid-body spring model (RBSM) (Kambayashi et al. 2020) of representative angular sectors of prototypical CBSs.

Based on the last two models, it was found that cracks mainly oriented perpendicularly to the radial direction form initially in the concrete cover facing the reactor cavity and further develop toward the interior of the wall. Kambayashi et al. found that restrained RIVE causes the formation of cracks up to 200 mm from the inner surface of the CBS. With prolonged operation, the average crack width (maximum width of ≤1 mm at 60 years of operation) gradually increases in the concrete cover but remains limited beyond the location of the reinforcement (< 5 μm). Hence, this model suggests two important conclusions. First, the effects of irradiation cause damage exceeding the location of the reinforcement. Thus, the load transfer between the concrete and the reinforcing bars (bond strength) is under question, although it is essential for effective reinforced concrete. However, "Rebars and creep suppress the growth of cracks that exceed 0.001 mm to approximately 100–150 mm from the inner surface" (Kambayashi et al. 2020). Second, the important crack width in the concrete cover calls the integrity of in-service irradiated concrete into question. "Delamination behavior due to the neutron-induced expansion of aggregate may suggest the risk of the reduction of shielding performance by spalling of the surface concrete" (Kambayashi et al. 2020). Similar conclusions were drawn by Giorla, Le Pape, and Huang (2016), although the damage depth was found only in the range of 80–150 mm, depending on the presence of creep and shrinkage in the model.

Full 3D models of prototypical water-water energetic reactor (VVER) and PWR CBSs were also developed and published by The Czech Technical University and Oak Ridge National Laboratory (Khmurovska et al. 2019; Cheniour et al. 2023), respectively:

*VVER*: Khmurovska et al. (2019) published the simulation results of a complete VVER-440/213 CBS using an FEM. VVER CBSs include a 70 cm thick serpentine-based concrete shield facing the reactor cavity and a 2.5 m thick structural concrete wall. Irradiation-induced, thermal, and mechanical damages were accumulated using an approach similar to that employed by Pomaro et al. (2011). Irradiated concrete properties followed the suggestions from Le Pape (2015). Mazars' model was assumed to account for mechanical damage (Mazars and Pijaudier-Cabot 1989), and the B3-model was used to represent creep (Bažant and Jirásek 2018). The simulation results show the formation of vertical cracks propagating from the top of the CBS where the thickness was reduced. (This geometry is not representative of US PWR CBSs). These cracks were caused by the gradual "vase"-shaped deformation induced by the expansion of the serpentine shield and the reduction of the concrete section toward the top of the CBS.

*PWR*: The details of the model are provided in the next section. The model geometry includes the hollow cylindrical CBS which measured 4 m high and 2 m thick and which was connected to a "rigid" 2 m thick basemat. Vertical and hoop #8 reinforcement bars were located at a 3 in. depth. The inner surface of the CBS was lined with 5 mm thick carbon steel plate. Fluence fields were calculated with the code VERA-Shift. The concrete constitutive model is mostly comparable to that employed by Khmurovska et al. (2019). Damage penetrates inside the CBS to reach the reinforcement bar location

at approximately 60 years of operation. Because of the absence of structural constraint at the top of the CBS, the overall deformation of the CBS takes the shape of a vase, but the constant thickness of the CBS prevents the formation of vertical cracks along the radial planes as observed in the VVER model previously discussed.

In summary, the varied aging structural model of the CBS was subjected to in-service irradiation using different modeling strategies (semi-analytical, finite element, discrete approach), all leading to similar conclusions:

1. Irradiation-induced damage in concrete is caused by two concurrent mechanisms: (1) *intrinsic* damage caused by formation of voids and cracking in the concrete constituents as observed on a concrete specimen subject to free expansion, and (2) the *structural* damage caused by excessive stresses in the region subject to high fast-neutron fluence toward the reactor cavity. These excessive stresses occur in the vertical and orthoradial directions and are caused by structural constraints associated with the cylindrical geometry of the CBS and the attenuation profile of fast neutrons moving radially toward the back of the CBS.
2. Although the damaged depth varies from one model to another because of differences in the parameters used in the RIVE, damage, and creep constitutive laws, all models indicate that damage extends to or beyond the location of reinforcement. This observation questions the integrity of the steel–concrete bond during accident conditions.
3. Cracks open mainly along the unrestrained radial direction in the region located near the reactor cavity. Crack opening width decreases with the CBS radius: larger cracks occur near the CBS surface. Minimal cracking occurs at or beyond the reinforcement location. This observation poses the question of possible spalling, notably during a loss of coolant accident (LOCA), an accident situation that will increase this risk.

### 2.1.5 Knowledge Gaps

**Fast neutron flux**

The main knowledge gap to date is regarding the role of the fast neutron flux on the RIVE rate. The JCAMP conducted a series of irradiation experiments on metachert, single quartz, granodiorite, and sandstone aggregates in various in-core positions of the LVR-15 reactor operated by centrum výskomu ŘeŽ (CVR) in the Czech Republic (Maruyama et al. 2025). The irradiation temperatures ranged from 45 to 62 °C, the dpa in quartz from 0.01 to 0.23, and the fast neutron flux from $4.9 \times 10^{12}$ to $17 \times 10^{12}$n.cm$^{-2}$ ($E > 10$keV). For comparison, the fast neutron flux at the surface of the CBS during operation is on the order of $10^{10}$ n.cm$^{-2}$. The rate of radiation-induced expansion was determined using XRD combined with Rietveld analysis, revealing a neutron flux dependency: higher neutron flux resulted in a higher rate of expansion. The authors hypothesized that the observed rate effect may be caused by defect-healing involving the diffusion of silica and oxygen, crystallization on the grain surface or interfaces, and facilitation of radiation-induced stress relaxation in the irradiated quartz. The authors noted that “The diffusion of dislocations, as well as Si and O, depends on the distance between neutron-irradiation-induced defects and the grain surface, rocks with larger grain sizes should exhibit a lower expansion rate."

A two-phase rate model of crystalline and amorphous phases is proposed by Maruyama et al. (2025) to interpret the RIVE data obtained at different fast neutron flux in the LVR-15 reactor (in-core positions). Interestingly, the activation energy of the healing reaction calibrated on Bykov et al. (1981) data is approximately 30 kJ mol$^{-1}$ K$^{-1}$. This value is consistent with the activation energy for the diffusion of Si and O during recrystallization (White 1977).

This model should be recognized as the first model capable of reconciling (1) expansion data obtained at comparable irradiation temperatures and varying neutron flux and (2) expansion data obtained at comparable neutron flux but varying irradiation temperatures. Nevertheless, there are two theoretical limitations that must be addressed. These will be discussed in a subsequent LWRS milestone report to be produced during FY25.

Additional research is needed to understand and model the effects of in-service fast-neutron flux. It remains to be established whether the apparent temperature-induced defect-healing involving the diffusion of silica and oxygen proposed by Maruyama et al. (2025) is a valid hypothesis. The increase of temperature in the irradiated specimens is dependent on the energy deposition caused by the neutron flux and the gamma ray dose rate. The irradiation-induced defects in ceramics and rock-forming minerals vary when exposed to ionizing (e.g., electron (Hobbs and Pascucci 1980; Pfeffer 1985), gamma (Imai et al. 1993)), or nuclear radiation. These effects are not necessarily cumulative. When ionizing radiation leads to a healing mechanism, it is referred to as *ionization-enhanced annealing (IEA)*.

**Other time-dependent mechanisms**

The interpretation of in-pile irradiation experiments and their extrapolation to in-service conditions in LWRs requires that all acceleration factors that may affect the irradiated materials be addressed. The identified time-dependent mechanisms associated with irradiation can be separated into two broad categories depending on the absence or presence of a liner in the CBS:

1. *Drying-induced phenomena* in unlined CBSs, including shrinkage, changes in thermal, irradiation transport, and mechanical properties of cement paste-bearing hydrates, drying creep, $CO_2$ diffusion, aerobic corrosion, and
2. *Time-dependent phenomena* occurring or enhanced at near-moisture saturation in lined CBSs, including basic creep, anaerobic corrosion, and dissolution-precipitation of cementitious or aggregate-bearing phases such as ASR or other reactive mechanisms.

The details of IAASR and IAC are discussed in sections 3.1 and 3.2, respectively.

**Creep under irradiation**

Creep of the cement paste may not be considered a valuable research subject because the in-service permanent loads applied to the CBS are low, and the CBS is not post-tensioned like some CCBs. Nevertheless, pending in-service RIVE formation, the cement paste is subject to stresses caused by expansion of the aggregate and the structural constraints detailed previously in the section titled *Structural Performance*. Whereas these stresses may cause cracking, relaxation mechanisms may result from viscous or viscoplastic relaxation processes. Here, the term *relaxation* designates the dual mechanism associated with viscoelastic creep. The existence of such relaxation mechanisms is supported by the absence of significant surface cracking in concrete specimens that were recently irradiated in the JEEP-II and LVR-15 reactors, despite the level of aggregate expansion at which ASR-subjected specimens would typically exhibit noticeable surface cracking patterns.

Very limited data on shrinkage and creep of irradiated cementitious materials are available in the literature (Gray 1971; McDowall 1971). Under 10 months of gamma irradiation at a dose of 0.114 kGy $h^{-1}$, McDowall (1971) found that the creep rate of concrete (10 MPa) decreases, whereas the shrinkage rate increases. The specimens were sealed in copper foils, although venting of radiolytic gas is permitted through a gas bubbler filled with water. Although moisture transport through vapor diffusion is not allowed, gas transport could lead to a partial, although limited, “drying” of the specimens. Hence, it can be assumed that, in the absence of better data, the effects on creep and shrinkage rates are primarily attributed to gamma-ray exposure. Gamma irradiation—induced hydrogen production from absorbed water and nano-confined water are, respectively,

two orders and one order of magnitude higher than that of bulk water in controlled nanopores (8–300 nm) of borosilicate glasses (Rotureau et al. 2005; Le Caër et al. 2005). The microstructure of C-S-H suggests that similar radiolytic effects could be observed in cement pastes, potentially causing changes primarily at the nanoscale. A possible irradiation-induced drying mechanism of absorbed and nanoconfined water could result in the collapse of C-S-H as observed after drying under sustained moderate temperatures (Jennings et al. 2007; Maruyama et al. 2014). Hence, such a mechanism could possibly cause an increase in the apparent viscosity and thus a decrease in the creep rate under gamma irradiation. Concurrently, radiolysis of absorbed water at the C-S-H surface can result in release of the disjoining pressure (Beltzung and Wittmann 2005) and hence an increase the shrinkage rate. Under concurrent neutron and gamma irradiation, shrinkage, and, subsequently, creep (6.9 MPa), Portland cement grout specimens were tested by Gray (1971) at temperatures ranging from 20 °C to nearly 95 °C. For approximately 15 days, the creep specimens were subjected to irradiation in the Herald test reactor (United Kingdom). Fast neutron fluence is not specifically reported but can be estimated at $\approx 0.75 \times 10^{19}$ n.cm$^{-2}$ with a flux of $\approx 5 \times 10^{12}$ n.cm$^{-2}$ s$^{-1}$. The energy cut-off is not specified.

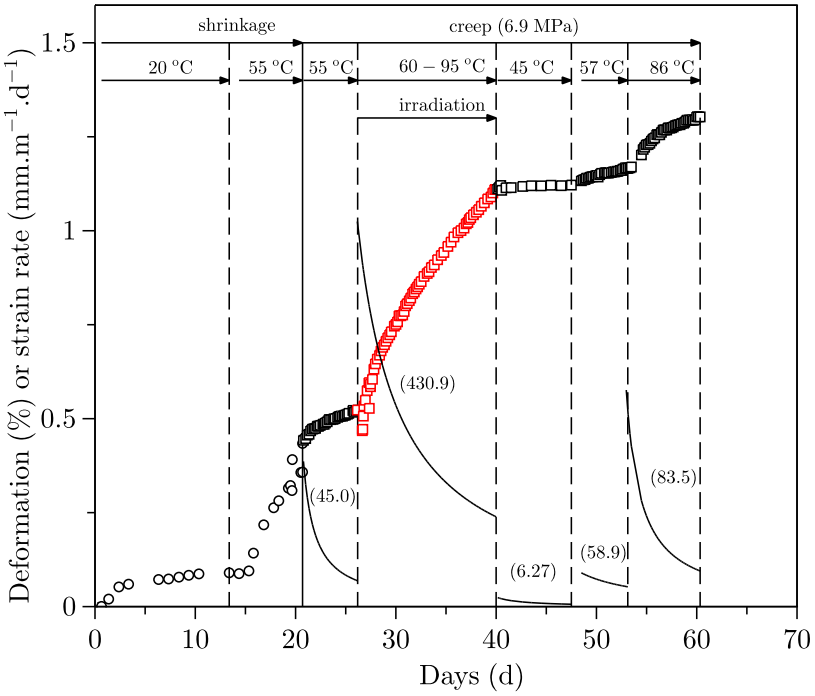


**Figure 1. Measured shrinkage (open circle) and creep (open square) strain of Portland cement grout; red open square corresponds to creep under neutron irradiation; reconstructed from Gray (1971) data; numbers in parenthesis indicate the creep kinetics parameter, solid line: creep kinetics.**

The deformation history reconstructed from Gray's data is presented in Figure 1. The creep data are simply interpreted using a logarithmic model:

$$\varepsilon = \varepsilon_0 + a \log\left[1 + \frac{(t - t_0)}{\tau}\right],$$

where $a$ (μm m$^{-1}$) is a fitted kinetics parameter, and $\tau$ is the characteristic time, arbitrarily set to 1 day for the

sake of comparing the kinetics parameters across the different stages of the experiment. Creep kinetics at 60–95 °C (average of ≈ 70 °C) under concurrent irradiation are one order of magnitude higher (430.9) than the creep of specimens out of pile before (45.0) or after irradiation (< 83.6) in a similar temperature range. The relative humidity and loss of mass of the specimens were not monitored. Neutron-induced radiolytic effects on water are similar in nature to gamma-ray effects (Kontani et al. 2010) and thus should lead to a decrease in the creep rate following the observation of McDowall (1971). This indicates the possibility of an additional mechanism, even though experimental data support that neutron irradiation has a limited effect on the macroscopic mechanical properties of cement paste (Gray 1971; Elleuch, Dubois, and Rappenau 1971; Elleuch, Dubois, and Rappeneau 1972). The possible mechanisms of neutron-induced damage to the solid phase of cement hydrates remain poorly understood and require further investigation. Pignatelli, Kumar, Alizadeh, et al. (2016) proposed that a dissolution-precipitation mechanism is at the origin of C-S-H assemblage creep mechanism in a moist non-drying environment. Although no specific data are available documenting the effects of irradiation on the dissolution rate of C-S-H in alkaline solution, it was observed that irradiation enhances the dissolution rate of rock-forming silicates.[7] If such an effect were demonstrated, then it would be possible to hypothesize that neutron-irradiation increases the creep kinetics of the cement paste.

However, it must be recognized at this point that, aside from the proposed dissolution-enhanced creep kinetics, the mechanism(s) behind creep remain a source of debate in the scientific community.

It is expected that the characterization of in-service irradiated concrete will not provide direct evidence of irradiation-enhanced relaxation, aside from the interpretation of existing cracks in the harvested specimens, for three main reasons:

1. In situ relaxation will result from aggregate RIVE and structural constraints, which cause vertical and hoop stresses. Assessing the local stress state in the cement paste hydrates will involve uncertainty and will require advanced micro-/meso-scale modeling.

2. Any attempt to measure creep relaxation properties on harvested concrete specimens using techniques such as nano-indentation will be limited to the effects caused by the irradiation dose, not the dose rate. The latter cannot be replicated.

3. Creep properties are influenced by moisture content and temperature. Replicating in-situ conditions may be challenging.

In summary, the study of expected neutron-irradiation-enhanced relaxation is anticipated to be addressed by combining in-pile instrumented creep tests with advanced MD modeling. The irradiation experiment could be based on numerous in-pile graphite creep experiments (Campbell 2018).

**Drying-induced irradiation transport**

Because hydrogen is the main contributor to neutron stopping, the loss of moisture caused by drying affects the penetration of fast neutrons in the CBS. Drying occurs as moisture in the concrete is transported toward the reactor cavity when the CBS does not have a metal liner to prevent convection at the surface of the concrete. The drying rate is a function of several factors, including the initial water content in the concrete mix, the porosity distribution affecting moisture transport, the radiolytic gas production rate, the operating temperature of the concrete, and the convection conditions in the cavity, which may be influenced by forced venting. Full coupling of irradiation transport, moisture transport, and radiolytic effects has never been achieved to date, primarily because the radiolytic effects of the various water forms in concrete, which involve complex chemical interactions (Bouniol 2004, 2010), remain complex. Coupling temperature and moisture

7. This subject is addressed in the section titled *irradiation-assisted alkali-silica reaction (IAASR)*.

transport in concrete models can be found in the literature (Bažant, Chern, and Thonguthai 1982; Giorla, Le Pape, and Huang 2016).

Parametric irradiation transport studies such as that presented in Risner, Alpan, and Yang (2020) illustrate the importance of this question on the extent of fast neutron profile ($< 10^{19}$ n.cm$^{-2}$ at $E > 0.1$ MeV) in the CBS.

## 2.2 CORROSION

### 2.2.1 Reinforcement and liner

Concrete reinforcing bar ("rebar") is typically made of 0.04%–0.30% low-carbon steel mostly in the form of pure iron and ferrite with only trace amounts of alloys and impurities. As described by Graves et al. (2014),

> *Most of the mild, or conventional, reinforcing steels used in NPPs to provide primary tensile and shear load resistance/transfer consist of plain carbon steel bar stock with deformations (lugs or protrusions) on the surface. These bars typically conform to ASTM A 615 or A 706 specifications (initial plants may contain bars conforming to ASTM A 432 or A 305 specifications that have been either replaced by the above or withdrawn).*

The drywell portions of BWR and PWR containments are typically lined with carbon steel (ASTM A 36 or A 516) (Graves et al. 2014).

### 2.2.2 Mechanisms

#### Half-cell

Corrosion of steel reinforcement embedded in concrete proceeds from two half-cells located at a small (micro-cell) or larger distance (macro-cell).

Varied anodic reactions (dissolution or oxidation of iron) are possible: $Fe \longrightarrow Fe^{2+} + 2e^-$, $3Fe + 4\,H_2O \longrightarrow Fe_3O_4 + 8\,H^+ + 8\,e^-$, $2\,Fe + 3\,H_2O \longrightarrow Fe_{203} + 6\,H^+ + 6\,e^-$ or $Fe + 2\,H_2O \longrightarrow HFeO_2{}^- + 3\,H^+ + 2\,e^-$ (Hansson 1984). The formation of $Fe_{203}$ and $Fe_{304}$ occurs in concrete at normal pH (see next paragraph on passivation). Electron production requires balancing of cathodic reactions such as $2\,H_2O + O_2 + 4\,e^- \longrightarrow 4\,OH^-$ (or $2\,H^+ + 2\,e^- \longrightarrow H_2$ in anaerobic corrosion). Further diffusion of $OH^-$ toward the anodic half-cell can also lead to the precipitation of iron hydroxides: $Fe^{2+} + 2OH^- \longrightarrow Fe(OH)_2$.

#### Passivation

Steel reinforcement is embedded in concrete to ensure proper mechanical bonding: the transfer of loads between steel in concrete that is essential to provide structural performance in tensile regions. The concrete provides protection of the reinforcement by creating a (thick) coating that limits the access of water and oxygen to the steel surface and providing a stable (insoluble) alkaline environment for corrosion products (Hansson, Poursaee, and Jaffer 2012). At the early age of concrete ($\approx$ 7 days) (Poursaee and Hansson 2007), a passive layer of iron in alkaline media is formed around the reinforcing bar. This passive layer is made of magnetite ($Fe_3O_4$, also known as black iron oxide) and maghemite ($\gamma$–$Fe_2O_3$), both of which share the same the same spinel ferrite structure, thus making it possible for substitution $3Fe_3O_4 \rightleftharpoons 4\gamma\text{–}Fe_2O_3 + Fe^{2+} + 2\,e^-$ (Andrade et al. 2001). The thickness of the passivation layer is a few nanometers. Because of the saturation of $Ca(OH)_2$ and the presence of $K^+$ and $Na^+$ in the pore solution, the high pH (12–13) provides a stable environment for the thin layer of corrosion products: hence the term *passivation*. Under that state, the corrosion-induced rate of steel loss is estimated to be in the range of 0.1 to 1.0 $\mu m\,yr^{-1}$. Such a value is considered too low to be detrimental to the performance of reinforced concrete, even after decades on service life. Therefore, deleterious corrosion requires a change of corrosion rate (e.g., governed by pH drop) or the degradation of the passivation layer (e.g., chloride attack). Carbonation and chloride ingress are detailed in the following sections

Another consideration involves the absence of a normal passivation layer caused by the presence of unexpected objects such as framework wood pieces or worker's gloves inadvertently left or dropped in the fresh concrete during construction. When these objects are in contact with steel, they prevent the initial formation of a passive layer, provide a source for oxygen, and create a macrocell at the origin of local corrosion. This type of mechanism has been observed in several cases of containment steel liner in NPPs (Petti et al. 2011).

Note that bacteriological attacks can also lead to corrosion. This topic is not considered in this review because it is not expected to affect critical NPP components such as the containment building, the spent fuel building, or the primary biological shield.

#### Carbonation

Carbonation-induced corrosion is the most evident and understood mechanism. Acidic atmospheric gas such as carbon dioxide slowly diffuses in the gaseous or dissolved forms through the concrete porous network. Reaction with calcium hydroxides (e.g., Portlandite and other hydroxides) causes the formation of calcite, $Ca(OH)_2 + CO_2 \longrightarrow CaCO_3 + H_2O$, and participates to the neutralization of the pore solution (Hansson, Poursaee, and Jaffer 2012). Within the carbonation front, the pH drops to approximately 8, and the oxides forming the passivation layer become unstable, thus causing active corrosion (Pourbaix 1966). The development of carbonation-induced corrosion is governed by the diffusion rate of carbon dioxide which depends on the atmospheric $CO_2$ content, the permeability of the concrete, and the thickness of the concrete cover protecting the reinforcement. The diffusion of carbon dioxide in concrete depends on the moisture content, which also affects the precipitation of calcite. The maximum penetration rate occurs in the range of 50–70% relative humidity. The precipitation of calcite and the release of water promoting further hydration of unreacted cement decrease the carbonation penetration rate.

#### Chloride attack

Excess chlorides are present in marine environments and in soils when deicing agents are used in northern regions. The presence of chloride in the concrete mixture is the result of malpractice (e.g., use of untreated seashore sand). This situation is not of concern for LWRs. Hence, chlorides diffuses from the external surface of the concrete. The time at which an adverse concentration of chloride occurs in the vicinity of the embedded reinforcement depends on the thickness of the concrete cover; the concentration of chlorides in the environment; the diffusion properties in the concrete, which depend on the pore structures and the ability to bind chemically chlorides in the cement; the temperature; and the moisture content in the concrete.

### 2.2.3 Properties

Once corrosion is initiated, the formation of oxides around the reinforcement bars is associated with the reduction of the steel cross section, thus resulting in a decrease in the mechanical performance of the reinforcement: loss of yield strength (Morinaga 1990; François, Khan, and Dang 2013; Lee, Tomosawa, and Noguchi 1996; Xia et al. 2013), tensile strength (Almusallam 2001; Apostolopoulos, Demis, and Papadakis 2013; Fernandez, Bairán, and Marí 2015; François, Khan, and Dang 2013; Xia et al. 2013), and maximum elongation (Almusallam 2001; Ouglova et al. 2006). The density of the oxide precipitates is lower than that of pristine steel. The volume change of the oxide layer around the reinforcement affects the bond strength of the embedded steel in concrete (Almusallam et al. 1996; Cabrera 1996; Bhargava et al. 2007).

Although the oxides initially fill the defects between the concrete and the steel, causing the bond strength to increase, the increasing built-up pressure damages the concrete and leads to a loss of bond associated with the formation of corrosion products.

As a result of the formation of oxidation products around the corroding steel reinforcement, the lateral pressure generates tensile stresses in the surrounding concrete. At a later stage, cracks may develop in the surrounding concrete through the concrete cover, toward the surface parallel to the reinforcement, or in the form of delamination along the reinforcement bars. The development of concrete cracking depends on the tensile strength of the concrete and the confining effect; the path of weakest resistance is generally through the concrete cover toward the outer surface of the reinforced concrete element.

### 2.2.4 Structural significance

It is widely recognized that corrosion of embedded passive or active reinforcements is the major source of maintenance expense—on the order of magnitude of several billion dollars per year—in civil structures ( including structures for transportation, power distribution, and power generation). Hartt, Lee, and Costa (1997) provides a comprehensive breakdown of the overall costs of corrosion in the different sectors.

#### Chloride attack

"All reinforced concrete structures that are in contact with seawater or exposed to wind-driven ocean spray are at risk of corrosion-induced deterioration caused by the ingress of chloride ions" (Chapter 5 of ACI 222.3R-03 [2003] identifies which structures are most susceptible to carbonation or chloride-induced corrosion when in direct contact with concrete.)

As a result, all reinforced or prestressed concrete structures built in coastal areas are vulnerable to chloride attack. This includes containment buildings, intake structures, essential water service piping (if made of concrete), and more generally, any buildings interacting with the external environment. The ground can also contain additional chloride, which may lead to significant damage to inaccessible parts of the structure, such as buried pipes, containment basemat, and other below-grade components of nuclear island structures.

"All areas exposed to de-icing salts used for winter maintenance of roads or pedestrian pathways are vulnerable. These salts quickly penetrate concrete and can lead to significant deterioration. Such damage is generally confined to areas involved in ground transportation and pedestrian access. In this context, a report by the US Geological Survey [Mullaney et al., 2009] discusses the widespread use of deicing salts in northern states:

> *Salt usage in the United States has increased since the 1950s, growing from 42.9 million tons in 1975 to nearly 58.5 million tons in 2005. Historically, the largest consumer of salt has been the chloralkali industry. However, in 2005, the largest use of salt was for de-icing (39.5 percent), followed by its use in the chloralkali industry (34.7 percent). The remaining 25 percent was allocated to other uses. About 76 percent of the shipments of evaporated and rock salt were directed to the Northern States, which are part of the glacial aquifer system. Chloride concentrations exceeded the U.S. Environmental Protection Agency's secondary maximum contaminant level (SMCL) of 250 milligrams per liter in 2.5 percent of samples taken from 797 shallow monitoring wells (land-use wells) and in 1.7 percent of samples from 532 drinking-water supply wells sampled between 1991 and 2003. The highest chloride concentrations were found in samples from shallow monitoring wells in urban areas (median concentration of 46 milligrams per liter), followed by agricultural areas (median of 12 milligrams per liter) and forested areas (median of 2.9 milligrams per liter).*
>
> *Interestingly, the chloride concentrations reported in groundwater are comparable to the limits specified by ACI 318-08 [2008, Table 4.3.1, pp. 318–358], indicating that such environments could be highly aggressive to reinforced concrete structures.*

#### Operating experience

Several cases of corrosion in NPPs concrete structures have been reported:

- The Koeberg Nuclear Power Station is located on the seashore of South Africa near Cape Town. The chloride content creates adverse conditions, causing corrosion of several concrete structures, including the delamination of the concrete cover of the containment buildings. The plant operator, Eskom, conducted extensive repairs and implemented cathodic protection to mitigate this issue.

- The Palo Verde Nuclear Power Station is located in a desert area of Arizona. This plant uses treated municipal water from the city of Phoenix to provide cooling. The water has a high chloride content, resulting in corrosion of the piping system and the mechanical draft cooling towers. The operator, Arizona Public Service, conducted extensive repairs, including replacement of the towers' prestressed fill beams with epoxy-coated reinforced beams, and they implemented cathodic protection on the main structural elements, including the columns supporting the fan deck.
- Engie-Electrabel noted deterioration in the concrete ceilings and walls of the bunkerized buildings in 2017 during planned shutdowns of the Tihange-3 and Doel-3 plants. Similar concrete degradation issues were discovered at Tihange-2 and Doel-4. Tihange-3, Doel-3, and Doel-4 have all returned to operation.
- Other instances were reported in France (underground lined reinforced piping), the United Kingdom (marine intake structures), and Canada (containment buildings).

**Impacts**

The main driving impacts of corrosion on the bearing capacity of reinforced concrete structures are the loss of steel section and ductility, the reduction of bond strength, the loss of cover in compression, the delamination of cover of the reinforcement bars in tension, and increased risk of buckling of compression reinforcement.

### 2.2.5 Knowledge Gaps

Corrosion of reinforced and pre-tensioned concrete elements is well understood and documented. The main knowledge gaps relate to the evaluation of the actual degree of degradation (inspection and nondestructive testing) and the assessment of structural integrity (Graves et al. 2014). The possibility of corrosion on the inaccessible side of the steel liner of the CCB, or the portion of the liner embedded in concrete, remains difficult to assess, primarily because of the lack of an easily deployable in-service inspection technique.

## 2.3 ALKALI-SILICA REACTION

### 2.3.1 Mechanisms

#### 2.3.1.1 Chemistry

ASR is a chemical reaction involving reactive silica in the aggregate and alkali that is generally released from the cement and present in the capillary pores of the hardened cement paste after hydration. The reactive mechanism is described in the literature (Glasser 1992; Miura and Ichikawa 1996; Ichikawa and Miura 2007). The principal alkali present in the pore solution are sodium, potassium, and calcium ions in equilibrium with hydroxyl ions which can diffuse through the concrete microporous network. *Reactive silica* refers to poorly crystallized (e.g., cryptocrystalline quartz) or amorphous forms of silica (as opposed to well arranged crystallized form such as $\alpha$-quartz).

Many types of aggregates may be susceptible to ASR, including quartzite, gneiss, siliceous limestone, graniodiorite, granite, monzonite, opaline, flint, chert, sandstone, greywacke, and basalt, to name a few (Poole and Sims 2017). Leemann and Takayma (2021) associate the reaction kinetics with reactive minerals:

- Early-expansive: opal, cristobalite, tridymite, rhyolitic glass
- Intermediate expansive: some volcanic glass, chalcedony, cryptocrystalline quartz
- Late-expansive: cryptocrystalline quartz, microcrystalline quartz
- Extremely late expansive: microcrystalline quartz in quartzite, gneiss and granite

The disorganized silicate microstructure weakens the siloxane bond (Si−O−Si).

$$\equiv \mathrm{Si{-}O{-}Si} \equiv + \mathcal{A}^{+} + \mathrm{OH}^{-} \rightarrow \equiv \mathrm{Si{-}O{-}}\mathcal{A} + \underbrace{\mathrm{H-O-Si}\equiv}_{\text{silicic acid}}, \tag{1}$$

where $\mathcal{A}^{+}$ designate alkali, typically, $Na^{+}$ or $K^{+}$, in the pore solution. These alkali find their origin mainly from the cement. Their content varies with the cement phases proportions, the kiln temperature, feed rates, and oxidizing/reducing conditions in the kiln. A secondary source of alkali may come from silicate-bearing aggregate (Lagerblad 2012).

Under the attack of hydroxyl ions, hydrolysis of silica occurs, causing the formation of alkali-silicate gel through the substitution of silicon by any of the alkali ions mentioned previously, and silicic acid, as shown in Eq. (1). The kinetics of this reaction are governed by the degree of the disorder of the silicates. Ion irradiation–induced amorphization greatly increases the dissolution rate of originally ASR-resistant silicates (Ichikawa and Koizumi 2002; Ichikawa and Kimura 2007; Pignatelli, Kumar, Field, et al. 2016; Hsiao et al. 2017; Hsiao et al. 2018). In those experiments mimicking the effects of neutron irradiation, the dissolution rate is measured before and after irradiation by placing the specimens in contact with an alkaline solution.

Silicic acid then immediately reacts with alkali and hydroxyl ions to form further alkali-silicate gel, as shown in Eq. (2). The latter is highly hygroscopic. In Eqs. (1) through (3), $\mathcal{A}^{+}$ denotes alkali ions, primarily $Na^{+}$ and $K^{+}$.

$$\mathcal{A}^{+} + \mathrm{OH}^{-} + \mathrm{H{-}O{-}Si} \equiv \rightarrow \equiv \underbrace{\mathrm{Si-O-}\mathcal{A} + \mathrm{H_2O}}_{\text{oligomeric alkali silicate}} \tag{2}$$

By capturing water from the pore solution shown in Eq. (3), an expansive alkali-silica gel is formed which gradually fills the material porosities. A sufficient amount of water can be obtained if there is a liner at the surface of the CBS. The stability of neo-formed alkali-silica gel under irradiation—the radiolytic effect—is largely unknown.

$$\equiv \mathrm{Si{-}O}\mathcal{A} + \mathrm{nH_2O} \rightarrow \equiv \underbrace{\mathrm{Si{-}O^{-}--(H_2O)_n{+}}\mathcal{A}^{+}}_{\text{expanded silica gel}} \tag{3}$$

#### 2.3.1.2 Moisture and Temperature

By comparing measurements of field concretes with the threshold level and environmental field conditions, Stark (1991) found that RH values greater than 80%, referenced to 21–24 °C, are required to support expansive alkali-silica reactivity (ASR). A similar RH value, under which ASR appears to stop, was reported by Jensen (2004). Such a high level of RH is found in structures in permanent contact with water (e.g., tertiary cooling circuits, river and sea water intake, below-grade structures in contact with ground water) and in massive structures, including plain or reinforced thick concrete components such as the CCB or the CBS. In those structures, the humidity varies in the thickness of the wall because of drying that occurs at the surface.

In internal LWR structures, the temperature of the air is above ~ 40 °C in operation. The design temperature limit per ACI 349 code is approximately 65 °C, with local deviation ranging up to approximately 90 °C in regions near penetrations and hot pipes. It was reported that operation temperature[8] near the RPV nozzle support was about 55 °C.

The RH and temperature of concrete structures were monitored in several Swedish LWRs, including Ringhals Unit 1 (ABB-I BWR), Forsmark Unit 2 (ABB-III, BWR-2500), Forsmark Unit 2 (ABB-III, BWR-3000), and Ringhals Unit 4 (3-loop PWR) using measurement probes (`HMP 110`) from *Vaisala Oy*. The monitoring duration lasted between approximately 250 and 400 days. The probe measured RH with a Vaisala HUMICAP© 180R sensor and measured temperature with a Pt1000 RTD, 1/3 Class B IEC 751 (Oxfall 2016). Probes were embedded at varying depths in different locations, including the CCB and internal concrete structures.

The measurements at Ringhals 4 started in August 2012 and were conducted until May 2013, approximately 30 years after operation began in November 1983. Measured RHs varied with depth as a result of drying at the surface, indicating that there was no metal liner at the surface of the CBS. Concrete temperature was largely independent of sensor depth for all internal structures (~ 30 °C in the basemat and ~ 40 °C in the "basin" wall), whereas a measured difference of approximately 10 °C was observed across the measured depth in the CCB wall. The measured RH was found to be higher than 80% at depths greater than 20 mm, 150 mm, and 240 mm, depending on the location. An accurate interpretation of the monitoring data would require a coupled heat transport and moisture transport model.

Water content analysis of cored concrete specimens from a 1.5 m thick internal wall at Hamaoka Unit 1 (BWR, operated between 1974 and 2009, cores taken in 2016) concluded that the RH was about 80% in the very middle of the wall (Rymeš et al. 2019).

However, it can be concluded that RH remains high in internal thick concrete nuclear structures, despite being exposed to moderate temperatures (> 30 °C) and low air RH (~ 25%). This finding also implies that moisture content in concrete protected by a metal liner will remain very high because drying can only occur at the opposite unlined surface.

Hence, environmental conditions favorable to ASR are expected to be mainly found in NPPs at two types of locations: (1) below-grade structures in contact with groundwater, and (2) behind lined, thick concrete walls. This statement does not exclude other locations, such as concrete structures exposed to natural environmental conditions. However, it is expected that the development of ASR will not be as exacerbated as in the two situations highlighted previously.

### 2.3.2 Properties

#### Gels

The effects of ASR on the structural properties of concrete depend on the expansion properties of the gel, the time-dependent mechanical properties of the gel, and the location of the gel. These three factors are the

8. Presentation from Pr. Maruyama at the International NEA-NRC workshop on concrete harvesting, Rockville, MD, October 2, 2024.

origin of local stresses that may lead to the formation of microcracks which may extend and form larger cracks at a later stage.

**Gel formation**

According to petrographic and SEM examination, Leemann and Takayma (2021) distinguish five stages:

i Formation of reaction rim, no cracks. However, there is also evidence that the formation of ASR products is initiated in preexisting aggregate pores (sub-micron scale) directly adjacent to the cement paste (Leemann 2022; Giebson and Seyfarth 2025). Thus, step (i) could possibly result from micro-exudation.

ii Rimming of ASR sol/gel (halo) in the cement paste around the reacted aggregate; deposits of gel within voids near the aggregates, with no cracks.

iii Cracking of the aggregate filled with ASR gel. There is no direct spatial superposition between the ASR products and the crack extent. Leemann (2022) notes: "Some aggregates crack, although the front has progressed only to a depth of a few hundred micrometers. Some aggregates have not cracked yet, despite the fact that the front has reached their center." This observation illustrates that ASR-induced aggregate cracking is governed by the presence of initial cracks and defects, the mechanical properties of the grain boundary (GB), and the expansion and stiffness properties of the gel.

iv Propagation of gel-filled cracks from the reacted aggregate into the surrounding cement paste. When aggregate cracking exhibits multiple microcracks, the gel may simply diffuse to fill existing adjacent pores in the HCP. When the aggregate cracking is dominated by a single major crack, the crack continues propagating into the cement paste up to a few millimeters). The ASR gel is typically crystalline within the aggregate cracks and amorphous within the HCP (Leemann 2022). At the extrusion stage, the aggregate cracks are mostly not filled with gel except in the region in contact with the cement paste. Subsequent crack filling is attributed to a plugging effect. During this phase, the filling gel is mostly crystalline.

v Increase in crack width and precipitation of ASR gel along cracks into air voids distant from the reacted aggregate.

vi Formation of a network of gel-filled cracks connecting the reacted aggregates.

**Gel evolution**

The reaction products of ASR, gels, and crystalline rosettes have similar compositions, irrespective of the type of aggregate: early or late expansive ASR, alkali silicate, or alkali carbonate reaction (Katayama 2014). The chemical composition of the ASR products may evolve with the stage of reaction and typically shows a partial replacement of alkali by calcium from the cement paste (Leemann and Takayma 2021), transitioning from Na-K-Ca-silicate hydrates (referred to as alkali-rich gels) to -Ca-silicate hydrates. At the final substitution stage, referred to as *the end-point of the reaction* or *the convergent point*, the ASR gel composition approaches that of non-expansive C-S-H gel (Katayama 2014) (mineral analogues: reyerite, gyrolite, tobermorite).

Alkali-rich gels crystallize in phyllosilicate rosettes with a continuous cation distribution of tetrahedral (8.0–8.5) and octahedral sites (4.0–5.5, O=20), ranging from cryptophyllite ($(KNa)_4Ca_2Si_8O_{20} \cdot 10\,H_2O$) and rhodesite ($KCa_2Si_8O_{18.5} \cdot 6.5\,H_2O$) to a solid solution of mountainite-shlykovite ($Ca_2Na_2KSi_8O_{19.5} \cdot 6.5\,H_2O$ to $(KNa)_2Ca_2Si_8O_{19} \cdot 7\,H_2O$). The calcium substitution appears to be driven by a diffusion mechanism that occurs between alkali and calcium at the boundary of the aggregate (Katayama 2014). Using cesium tracers, Leemann and Münch (2019) provided evidence—as confirmed by thermodynamic modeling (Guthrie and Carey 2015)—of calcium transport from the cement pore solution through the narrow ASR gel pre-filled crack, continuing the reaction toward the inside of the aggregate.

#### Gel viscosity

Two types of ASR sol/ gel—fluid alkali rich and viscous silica rich—coexist within same concretes: they form in equilibrium with relative humidity in concrete (Katayama 2014).

#### Gel expansion

Gel expansion is likely caused by the swelling pressure of water by ASR gel (Katayama 2014). The potential causes of stress generation by ASR products can be broadly categorized into swelling caused by water imbibition, osmotic swelling, crystallization pressure, mass accumulation within the aggregate, or a combination of these factors (Leemann 2022).

Note that the crystallization of rosettes from ASR gel does not appear to cause expansion pressure because (1) dehydration results in a volume decrease, and (2) rosette crystals are secondary forms growing within the ASR gel and are not a direct precipitate from aqueous solution (no crystallization pressure in supersaturated solution) (Katayama 2014).

Giebson and Seyfarth (2025) recently proposed a novel theory based on the colloidal nature of the gel which is summarized here. Colloidal (gel) nano-particles form inside the boundary of the aggregate and remain trapped inside by the Donnan effect (osmosis) (Donnan 1911; Kunitz 1928). The charge imbalance with the cement pore solution results in further diffusion of alkali inside the aggregate. Once charge balance is reached, water osmosis through the aggregate membrane causes damaging hydric pressure.

#### Concrete properties

Note: There is abundant literature on the effects of ASR on concrete properties. A summary is provided here for the sake of clarity.

#### Expansion

The macroscopic expansion caused by ASR follows a sigmoidal evolution over time (Larive 1997; Saouma and Perotti 2006). The characteristic parameters governing this sigmoidal evolution are specific to each concrete mix (Abd-Elssamd, Ma, Hou, et al. 2020) and to the relative humidity and temperature. The expansion rate appears to be controlled by thermal activation. The expansion rate decreases with RH. Below approximately RH $\approx$ 70%, expansion is not observed. The volumetric strain may not be distributed isotropically. Directions subject to compressive stresses caused by external loading or internal restraints (e.g., reinforcement) exhibit lower-to-negligible expansion (Saouma and Perotti 2006; Hayes et al. 2018).

#### Stiffness and strength

The mechanical properties of ASR-subjected mortar and concrete generally show decreasing trends with concrete expansion: expansion is associated with the formation of cracks, thus reducing Young's modulus and strength. The decrease in tensile strength and Young's modulus is more pronounced than the decrease in compressive strength (Abd-Elssamd, Ma, Le Pape, et al. 2020). Because ASR expansion is anisotropic (stress-controlled), the mechanical properties may not be isotropic either. This effect also includes the fracture properties of concrete (Hayes et al. 2020).

### 2.3.3 Structural significance

ASRs have been affecting thousands of concrete structures and infrastructures in the transportation and energy generation sectors—mainly hydroelectric dams because of the adverse humidity conditions. Several instances of ASR affecting NPPs throughout the world have been reported, including the turbine generator building foundation at Ikata-1, Japan (Shihoku Electric Power) (Takatura et al. 2005); the containment building at

Gentilly-1, Canada (HydroQuebec), the decommissioned graphite-gas reactor building in Saint-Laurent, France (EDF), and several concrete structures at Seabrook, NH (NextEra).

Information about ASR conditions at Seabrook can be found on the ADAMS database, the official record-keeping system through which the US Nuclear Regulatory Commission provides access to publicly available documents.

Several major research projects regarding the structural effects of ASR were conducted or are ongoing in varied institutions at National Institute of Standards and Technology (NIST) (Sadek et al. 2021; Thonstad et al. 2021; Weigand et al. 2021), at Institut de Radioprotection et Sureté Nucleaire (IRSN) (https://en.irsn.fr/research/odoba-project), and at ORNL (Hayes et al. 2018).

Because of the recent observations of ASR at the Seabrook Station NPP, demand for a better understanding of the mechanisms and effects of ASR in NPP structures has increased. Several studies have investigated the effects of ASR on the mechanical properties of concrete. Some studies have specifically investigated the effects of ASR on the shear strength of beams that are reinforced with stirrups as shear reinforcement (Seabrook Station Response to NRC letter to NextEra Energy Seabrook CAL No. 1-2012-002, 2013) (Saouma, Hariri-Ardebili, Le Pape, & Balaji, 2016). However, in a typical NPP thick wall structure, shear reinforcement is not required for structural strength as allowed by ACI 318 (ACI Committee, 2014) because the significant depth of concrete contributes to the shear resistance of the structural element. With the planar section of the wall being heavily reinforced for the predicted loads, this can lead to a severe case of anisotropic expansion from ASR. As ASR expands in the planar directions of the wall, the expansion is resisted by steel reinforcement. This anisotropy will drive the majority of the expansion in the unreinforced direction, leading to significantly different conditions than those of the concrete beam with both longitudinal and shear steel reinforcement. Experimental data on the effects of ASR in the specific case of a thick-walled concrete structures with no shear reinforcement are necessary to quantify the effect of ASR damage on typical NPP structural elements.

ASR primarily impacts the serviceability of a structure. Some of the most common issues associated with ASRs include misalignment of structures, displacement of equipment, and spalling at joints. The influence of ASRs on engineering properties is difficult to generalize, because both the rate and extent of expansion are influenced by factors such as the type of reactive aggregate, cement composition, cement content, structural constraints, and environmental conditions (Graves et al. 2014).

### 2.3.4 Knowledge Gaps

#### Swelling mechanism(s)

The varied hypotheses regarding the mechanisms of expansion caused by ASRs were summarized in 1993 by Helmuth et al. (1993). More recent theories can be found in the literature (Rajabipour et al. 2015) (Giebson and Seyfarth 2025).

Microstructural observations clearly show that stress is generated within the aggregates rather than in the cement paste (Leemann 2022). Although the potential origins of stress generation by ASR products can be attributed to swelling caused by water imbibition, osmotic swelling, crystallization pressure, mass accumulation, or a combination of these factors, no recent evidence allows for distinguishing between these mechanisms (Leemann 2022).

#### Swelling pressure

Environmental SEM observations of pre-existing gel-filled aggregate cracks provide evidence that gel expands as the RH increases (Leemann 2022). However, direct in-situ measurement results of the swelling pressure are not accessible.

Attempts to measure the swelling pressure in analytical experiments using synthetic gels (Struble and Diamond 1981; Gholizadeh-Vayghan 2017; Gholizadeh-Vayghan and Rajabipour 2017; Krüger et al. 2024) that provided valuable experimental designs have been criticized for using unrealistic ASR gel conditioning and pore solutions (Leemann 2022, 2025).

# 3. DEGRADATION SYNERGIES

## 3.1 IRRADIATION-ASSISTED ASR

### 3.1.1 Interaction between Operating Condition and Chemical Durability

In general, it is reported that the strength of concrete cores extracted from thick concrete walls in NPP structures exceeds the design properties due to the extended hydration of cement (Naus 2009). However, a chemical interaction between concrete and aggregates was recently reported in the Hamaoka harvesting project. Because of the relatively high temperature and moisture retention in thick concrete walls maintained over several decades, dissolution and precipitation of metastable cement hydrates and aggregate-forming minerals have been observed in harvested concrete cores at the Hamaoka NPP (Rymeš et al. 2019).

### 3.1.2 Effects of Irradiation on the Dissolution Rate of Silicates

**Single minerals**

The effects of irradiation on the chemical properties of quartz were first studied by Ichikawa and Koizumi (2002) using 200 keV Ar-ion irradiation. More recently, research sponsored by the Nuclear Energy University Program (NEUP), in coordination with the LWRS Program, provided additional data obtained from studying other minerals. Figure 2 summarizes the evolution of the dissolution rates across a range of pH levels as measured before and after ion irradiation on quartz ($SiO_2$, framework silicate), albite ($NaAlSi_3O_8$, feldspar, framework silicate) and almandine: ($Fe_3Al_2(SiO_4)_3$, garnet, island silicate) (Pignatelli, Kumar, Field, et al. 2016; Hsiao et al. 2017; Hsiao et al. 2018). All ion irradiations were conducted at the Michigan Ion Beam Laboratory (MIBL) using 400 keV-Ar bombardment at room temperature. The final ion dose was $10^{14}$ Ar cm$^{-2}$ in all cases. The dissolution rates of pristine and irradiated silicates tested can be approximated by linear expressions: $\log_{10}(D) \sim apH + b$. The corresponding values of $a$ and $b$ are given directly in Figure 2. Post–ion irradiation dissolution rates are always higher than pre-irradiation rates across the range of pH. At a given pH, the ratio of the post-irradiation dissolution rate to the pre-irradiation rate is almost independent of the pH for albite and almandine. Such a behavior is not observed with quartz. For the sake of comparison, these ratios calculated at pH 13 (the pore solution of OPC is higher than 12.5) are provided in Table 1. The irradiation-induced dissolution increase is one order of magnitude higher in albite than in almandine, and one order of magnitude higher in quartz than in albite.

**Table 1. Diffusion rates of quartz, albite, and almandine at pH 13 and 25 °C. D: unirradiated value, D$^*$: irradiated value. ($^\dagger$) Ichikawa and Koizumi (2002) estimated the increase at $\approx \times 700$.**

| Mineral | D (mol.cm$^{-2}$ s$^{-1}$) | D$^*$ (mol.cm$^{-2}$ s$^{-1}$) | D$^*$/D (-) |
|---|---|---|---|
| Quartz | $9.99 \times 10^{-15}$ | $2.12 \times 10^{-12}$ | $211.9^\dagger$ |
| Albite | $2.86 \times 10^{-13}$ | $4.41 \times 10^{-12}$ | 15.4 |
| Almandine | $6.35 \times 10^{-10}$ | $6.82 \times 10^{-10}$ | 1.1 |

Figure 3 shows the relationship between the ratio of post- and pre-dissolution rates and the density change for quartz, albite, and almandine. The maximum change of density of irradiated quartz, albite, and almandine is ≈-15% (Primak 1958; Zubov and Ivanov 1966), ≈-6% estimated from plagioclase RIVEs data (Denisov, Dubrovskii, and Solovyov 2012), and ≈-0.7% estimated from forsterite ($Mg_2SiO_4$), which is also an island silicate not categorized as a garnet but as an olivine. A general trend is observed: $\log_{10}(D^*/D) \sim -36\Delta\rho/\rho$, suggesting that the density change provides a macroscopic quantification of the formation of irradiation-induced defects (bond breakage), thus enhancing dissolution properties.

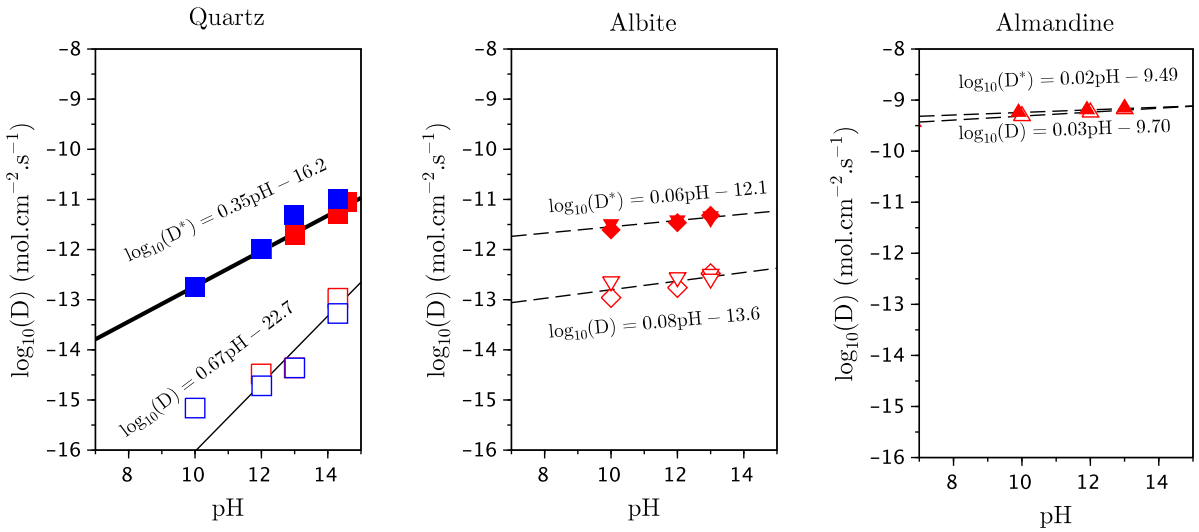


**Figure 2. Pre- and post-ion irradiation dissolution rate of quartz-001 (left) (Pignatelli, Kumar, Field, et al. 2016) at 25 °C, albite (center (Hsiao et al. 2017), and almandine (right (Hsiao et al. 2018). Empty and filled marks correspond to unirradiated and irradiated specimens, respectively. Solid filled blue marks indicate fumed silica. Solid filled blue marks indicate pulverized $\alpha$-quartz (MIN-U-SIL 10).**

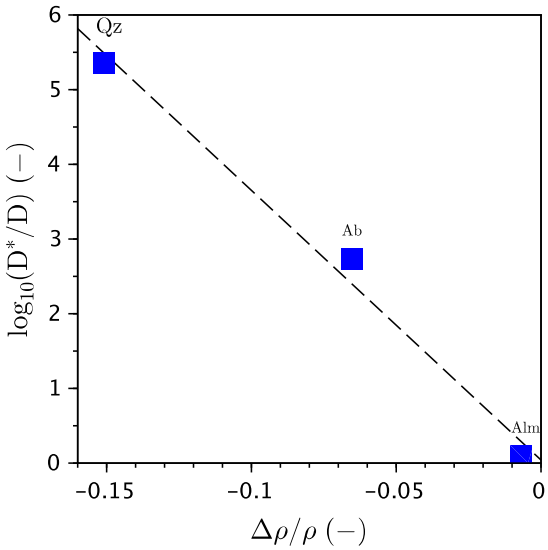


**Figure 3. Irradiation-induced dissolution coefficients (pH 13, $T$ = 25 °C) vs. density change.**

**Aggregate**

The only study of the effects of irradiation on the irradiation properties of rock was conducted at University of California at Los Angeles (UCLA) as part of a joint research activity with University of Tennessee Knoxville (UTK) and ORNL, sponsored by NEUP (Bouissonié et al. 2025).

The irradiated specimens included quartzite, limestone, and marble. Although quartzite and marble are not commonly used in nuclear concrete construction because of local aggregate sourcing, they present the advantage of being pure systems from the perspective of their chemical compositions. Quartzite contains exclusively quartz, the mineral most susceptible to RIVE. Marble is made of calcite, which is among the minerals least susceptible to RIVE. The studied limestone is mainly composed of a calcite matrix with embedded quartz inclusions.

The ion-irradiation used a 3 MV tandem accelerator to bombard the specimens with 5.5 MeV $He^+$ ions at room temperature. The total fluence was $2.5 \times 10^{17}$ ions.cm$^{-2}$. The estimated dpa calculated using the Stopping and Range of Ions in Matter (SRIM) code (Ziegler 1977-1985) are ~0.05, ~0.075, and ~3 dpa at the surface in the mid-range regions and in the peak damage regions, respectively. The total implanted depth reached approximately 23 μm

Post-irradiation examination included step-height measurements between unirradiated and irradiated regions, as well as dissolution rate measurements using VSI (with a resolution of approximately 3 nm). The average step height for the quartzite specimen was 0.97 ± 0.08 μm. No measurable dimensional change was observed in the irradiated marble specimen.

The far-from-equilibrium dissolution experiments were conducted using a NaOH solution at pH 13. Quartzite specimens were immersed for 24 hours at 90 °C, whereas marble specimens were tested in a flow-through cell at 25 °C. Pre- and post-irradiation dissolution rates exhibited nonuniform spatial distributions that were attributed to various factors, including grain orientation, surface roughness, and the presence of grain boundaries. Interpretation of the dissolution rate distributions in the form of probability distribution functions (PDFs) provides evidence of a peak indicative of fast dissolution, which appears to be associated with dissolution at the grain boundaries in the irradiated quartzite specimens.

The rates of of the pristine and irradiated mineral grain dissolution exhibit significant variations ranging from 0 to $1.5 \times 10^{11}$ mol cm$^{-2}$ s$^{-1}$, regardless of the time the dissolution experiment was conducted. Fitting the distributions in that range with common distribution functions (e.g., Gaussian functions) can only provide approximations. Two main broad "humps" in the data can be distinguished: the first, between 0 and $0.5 \times 10^{11}$ mol cm$^{-2}$ s$^{-1}$, is the most prominent, and the second is $\approx 1.0 \times 10^{11}$ mol cm$^{-2}$ s$^{-1}$. The origin of these two humps is not elucidated in the analysis. The dissolution rates associated with mineral grains are simply interpreted by calculating the mean values:

$$\langle D \rangle = \int_0^{2\times10^{-11}} \xi D(\xi) dD,$$

where $\xi$ is the number of counts (a.u.). The mean value of the dissolution rate of the pristine specimens is in the range of $0.32 \times 10^{-11}$ to $0.35 \times 10^{-11}$ mol cm$^{-2}$ s$^{-1}$, regardless of the time the dissolution experiment was conducted. The mean values of dissolution rates for the irradiated quartzite specimens ranged between $0.46 \times 10^{-11}$ and $0.52 \times 10^{-11}$ mol cm$^{-2}$ s$^{-1}$, with a decreasing trend over the course of the experiment. The ratio of the mean values of the irradiated specimens' dissolution rate to the pristine specimens' dissolution rate varies between 1.44 and 1.52.

The estimated dissolution rate of the pristine grain boundaries (GBs) was $4.68\times10^{-12}\pm3.81\times10^{-13}$ mol cm$^{-2}$ s$^{-1}$ at 48 h and $1.23\times10^{-11} \pm 1.06\times10^{-12}$ mol cm$^{-2}$ s$^{-1}$ at 90 h. It should be noted that a specific high dissolution

rate associated with GBs in the unirradiated quartzite specimen is more difficult to detect than in the irradiated specimen. The corresponding values for the irradiated quartzite are $1.04 \times 10^{-11} \pm 8.80 \times 10^{-13}$ mol cm$^{-2}$ s$^{-1}$ at 48 h and $3.29 \times 10^{-10} \pm 3.92 \times 10^{-12}$ mol cm$^{-2}$ s$^{-1}$ at 90 h. The increased dissolution rate at the GBs is attributed to RIVE-constrained damage, which causes the formation of microcracks. In this experiment, some quartzite grains chipped off. These grains were located at the surface having dimensions equal to or smaller than the irradiated depth. Ion irradiation–induced surface cracking patterns in polycrystalline aggregates cannot be considered representative of neutron irradiation-induced bulk cracking, even when comparing similar dpa levels. This is because the expansion induced by ion irradiation due to its shallow penetration is constrained by the pristine substrate (Bolse 1998; Harbsmeier and Boise 1998). As a result, significant lateral compression occurs, preventing the opening of surface cracks. Neutron-irradiated aggregates exhibit significant inter- and intra-granular crack and void formation (Maruyama et al. 2025). Hence, it can be hypothesized that under conditions similar to those tested by Bouissonié et al. (2025), the dissolution rate of the GBs would be accelerated if the aggregate were exposed to extended neutron irradiation.

**Table 2. Estimated dissolution rates of ion-irradiated aggregates (Bouissonié et al. 2025).[1]: pH = 13, $T$ = 90 °C. [b]: ratio of $\int \xi d\xi$.**

| Mineral/aggregate | $\langle D \rangle$ (mol.cm$^{-2}$ s$^{-1}$) | $\langle D^* \rangle$ (mol.cm$^{-2}$ s$^{-1}$) | $\langle D^* \rangle / \langle D \rangle$ (-) |
|---|---|---|---|
| quartzite | | | |
| Mean[1], 48 h | $0.35\times10^{-11}$ | $0.54\times10^{-11}$ | 1.52 |
| | | | 2.92[b] |
| Mean[1], 72 h | $0.35\times10^{-11}$ | $0.51\times10^{-11}$ | 1.44 |
| | | | 1.71[b] |
| Mean[1], 78 h | $0.35\times10^{-11}$ | $0.52\times10^{-11}$ | 1.47 |
| | | | 1.82[b] |
| Mean[1], 90 h | $0.32\times10^{-11}$ | $0.46\times10^{-11}$ | 1.44 |
| | | | 1.61[b] |
| Grain boundary[1], 48 h | $\sim 4.7 \times 10^{-12}$ | $\sim 1.0 \times 10^{-11}$ | 2.1 |
| Grain boundary[1], 90 h | $\sim 1.2 \times 10^{-11}$ | $\sim 3.3 \times 10^{-10}$ | 27.5 |

### 3.1.3 Effects of Increased Dissolution on the Possibility of ASR Gel Formation

In-service unirradiated feldspar-bearing rock exposed to extended periods of moderate temperature in NPP internal structures experiences gradual dissolution and the formation of calcium-aluminum-silicate hydrates (C-A-S-H) (Rymeš et al. 2019). Subsequent studies conducted by the JCAMP (International Committee on Irradiated Concrete (ICIC) communication) showed that ASR may form after prolonged durations exceeding the expected operation of nuclear generation stations. However, that study did not account for the effects of irradiation on the minerals' dissolution susceptibility. Nonetheless, it illustrates the metastable conditions occurring in operating NPPs that lead to phase changes.

Once the dissolution of silica occurs, the formation of ASR gel involves several mechanisms associated with the pore solution:

- Diffusion of alkalis (Na, K), hydroxides ($OH^-$), and calcium present in the pore solution, migrating toward the aggregate.
- Before late-stage crystallization, ASR gel is primarily present in the form of colloidal nanoparticles.
- Although the origin of the swelling mechanism is still debated (imbibition, osmosis), it involves water.

All the mechanisms listed above are related to pore solution diffusion or uptake. Water radiolysis, a major effect of irradiation, causes the dissociation of $H_2O$. Therefore, it is unknown whether the mechanisms involved in the formation, evolution, and swelling of ASR gel are affected by irradiation. This topic requires further research.

## 3.2 IRRADIATION-ASSISTED CORROSION

### 3.2.1 Experimental Evidence

Smart, Rance, and Werme (2008) conducted corrosion experiments of carbon steel wire under gamma irradiation in anaerobic conditions. This research pertained to the study of nuclear spent fuel disposals in geological repositories. The wire was exposed to an alkaline solution representing bentonite equilibrated water rich in $Na^+$ and $Cl^-$ at a pH of 10.4, which is lower than the normal pH in concrete. Other tests were conducted using an Allard groundwater solution (results not reported here).

A gamma irradiation experiment was conducted in a 60Co irradiator at dose rates of 11 Gy $h^{-1}$ or 300 Gy $h^{-1}$ (average energy 1.25 MeV) and a controlled temperature of 30 or 50°C at the Harwell facilities in Oxfordshire, United Kingdom.

At 50°C and 11 Gy $h^{-1}$, both tests in bentonite-equilibrated groundwater gave a higher corrosion rate that was initially compared to the results obtained previously under unirradiated conditions. At the beginning of the irradiation, the corrosion exceeded 10 μm $yr^{-1}$. However after ≈ 2,000 h, the corrosion rate was very similar to that measured in the absence of radiation, and after ≈ 4,000 h, the corrosion rate for both irradiated and unirradiated conditions was ≈ 0.05–0.2 μm $yr^{-1}$. At the higher dose rate (i.e., 300 Gy $h^{-1}$), the corrosion rate remained higher throughout the test, and after 5,000 h, the corrosion rate was ≈0.8 μm $yr^{-1}$ compared to 0.05 μm $yr^{-1}$ without radiation. Approximately 25% of this apparent increase in corrosion rate at 5,000 h was probably attributable to gas production from other materials within the cell apart from the steel, as shown by the dummy cell results. Nevertheless there appears to be a real increase in corrosion rate as a result of the high radiation. The corrosion products were mainly found to be magnetite ($3\,Fe + 4\,H_2O \longrightarrow Fe_3O_4 \downarrow + 4\,H_2 \uparrow$), along with FeOOH phases. At the end of the irradiation experiment, the solution pH decreased to about 9 independently from the dose rate.

Dewynter-Marty et al. (2017) conducted a gamma irradiation on 50 mm diameter cement paste cylinders with an 8 mm mild steel reinforcement (Fe500 grade using French grading system). Fifty specimens were prepared using OPC (CEM I) and sulfate-resistant cement (CEM V) and were cured at 20°C and 80% humidity for > 3 months. Nine specimens were placed in sealed containers in a 60Co irradiated at a low dose rate of ≈ 15 Gy $h^{-1}$. Some specimens were periodically removed after 3, 6, 9, and 12 months, corresponding to gamma doses of approximately 32, 68, 96 and 130 kGy, respectively. The corrosion currents measured after extraction from the irradiator do not appear to be correlated with the gamma dose: the maximum corrosion rate was < 1 μm $yr^{-1}$ at 6 months for CEM I specimens. The corrosion currents ranged between 0.1 and 0.2 μm $yr^{-1}$ for CEM-V specimens. Corrosion currents appear to be higher in CEM-I specimens than in CEM V specimens. This difference is attributed to the continuous, although, formation of oxygen in CEM-I specimens ($O_2$ partial pressure monitoring), whereas oxygen disappeared after 6 months of irradiation in the CEM V specimens. Oxygen consumption in CEM V specimens is attributed to a higher content of sulphur ions $S^{2-}$. The partial pressure of hydrogen increased continuously during the irradiation experiment.

The most comprehensive experiment to-date on the effects of gamma irradiation on corrosion of low carbon steel embedded in mortar specimens was published in Dabrowski et al. (2022). Mortar was prepared with either pure OPC (CEM I 52.5 R) or was blended with FA and limestone filler and 2 mm sand. The water-to-cement ratio was relatively high ($w/c = 0.6$) to create open porosity in excess. 6 mm low carbon (0.17 wt%) steel bars were embedded in 50 mm mortar cylinders (130 mm long). Bars were abraded with 4,000 grit SiC paper, sonicated, and air-dried to remove pre-existing corrosion products. The bars were coated with epoxy (corrosion inhibitor) except for a 10 $cm^2$ area embedded in mortar for electrochemical measurements. Testing included control plain mortar $40 \times 40 \times 160$ $cm^3$ prism specimens.

Specimens were cured in 20 °C water for 28 days. Specimens were placed in open metallic containers and cured for 24 h in a climate chamber at 65% RH and 1% $CO_2$ concentration to promote carbonation. The

containers were sealed with a metal lid after 24 h. Irradiation was conducted in the spent fuel pool of the Maria test reactor in Otwock, Poland. After 8 months of irradiation, the total gamma doses were estimated from thermoluminescent dosimeter readings (MCP-N type – LiF: Mg, Cu, P) and ranged between 1.7 and 1.9 MGy (average dose rate $\approx$ 0.3 kGy h$^{-1}$). The control specimens were kept at 38 °C to match that of irradiation conditions.

Pre- and post-irradiation testing included potentiodynamic polarization and electrochemical impedance spectroscopy (EIS) on the reinforced specimens, dynamic modulus, 3-point bending and compression strength, XRD (sampled from the core center), mercury intrusion porosimetry (MIP),[9] and nitrogen sorption on the unreinforced specimens.

The main findings were as follows:

1. *Mechanical properties*: The effects of gamma irradiation on bending and compressive strengths were limited to a change of a few percent points.
2. *XRD analysis*: The XRD spectra are quite similar for unirradiated and irradiated specimens. Gamma irradiation appears to promote carbonation as revealed by the reduction of Portlandite and the increase of the calcite peaks intensities. This observation is in agreement with previous literature results (Vodák et al. 2005; Vodák et al. 2011).
3. *Porosimetry*: Gamma irradiation caused an increase of pore volume varying according to the type of cementitious materials used in the mortar mix: 9% for the OPC specimens, 5% for the FA blended cement, and 20% for the cement blended with limestone fillers. In the OPC mortar specimens, the pore volume in the range of diameters between 0.1 and 1 μm increased, and those in the range of 0.01 to 0.1 μm decreased. Coarsening of the larger pores and the filling in the smaller pores were also observed by Vodák et al. (2011), albeit in different ranges that those reported by Dabrowski et al. (2022). Phenolphthalein testing conducted on fractured specimens did not reveal that the pH of the mortar around the steel reinforcement was significantly affected. This does not mean that a decrease of pH caused by radiation-induced carbonation did not occur.
4. *Potentiodynamic polarization*: The polarization curves shifted towards a lower corrosion potential ($-\Delta E$ ~0.13 to 0.26 V) and a higher corrosion current (×1.6 to 13) in irradiated specimens.

The relationship between the rate loss of reinforcement bar diameter and the corrosion current, $j_{cor}$, is given in μA cm$^{-2}$ using the relation $\Delta\phi/\Delta t \approx 0.023\, j_{cor}$ in mm yr$^{-1}$. The corrosion currents of the steel bar embedded in ordinary Portland cement are 0.02 and 0.24 μA cm$^{-2}$ for the unirradiated[10] and gamma-irradiated specimens, respectively, or about 0.5 and 5 μm yr$^{-1}$. Extrapolations of these rates led to 37 and 442 μm of diameter loss at 80 years assuming a constant corrosion rate.

Table 3 gives a summary of the corrosion rates measured on gamma-irradiated carbon steel embedded in cementitious matrix or pore solution as reported in Smart, Rance, and Werme (2008), Dewynter-Marty et al. (2017), and Dabrowski et al. (2022):

- Gamma irradiation accelerates the corrosion rate in aerobic and anaerobic conditions. An increase of the corrosion rate by an order of magnitude has been observed.
- The corrosion rate in anaerobic conditions appears to be correlated with radiolytic gas formation and hence decreases over time (Smart, Rance, and Werme 2008). Data are insufficient to draw conclusions about the correlation between the radiolytic rate and corrosion in aerobic conditions.
- Radiolytic gas production is accompanied by a reduction of pH in anaerobic conditions.
- Corrosion products mainly contain magnetite.

9. Drilled cores: diameter 9 mm, length 20 mm, after drying at 50 °C until a constant mass
10. The corrosion rate of passivated steel is 0.116 μm yr$^{-1}$ (Hansson, Poursaee, and Jaffer 2012).

**Table 3. Corrosion rate of carbon steel embedded in cementitious matrix/pore solution exposed to gamma irradiation.**

| Medium | Dose rate ($Gy\,h^{-1}$) | Dose (kGy) | Temperature (°C) | Condition | Corrosion rate[(#)] ($\mu m\,yr^{-1}$) | Reference |
|---|---|---|---|---|---|---|
| Bentonite | 11 | 0.45 | 30 | Anaerobic | $> 15$ ($\approx 5$)[(*)] | (s) |
| Solution | | 0.90 | 30 | | $\approx 0.15$ ($\approx 0.15$) | |
| | | 1.8 | 30 | | $\approx 0$ ($\approx 0$) | |
| | 300 | 12.5 | 50 | Anaerobic | $\approx 15$ ($\approx 5$)[(**)] | (a) |
| | 300 | 25.0 | 50 | | $\approx 1.5$ ($\approx 0.2$) | |
| | | 50.0 | 50 | | $\approx 0.9$ ($\approx 0$) | |
| | | 75.0 | 50 | | $< 0.5$ ($\approx 0$) | |
| CEM I paste | 15 | 130 | 25 | Aerobic (80% RH) | $< 0.25$ | (b) |
| CEM V paste | | | | | $< 0.1$ | (b) |
| CEM-I mortar | 300 | 1,800 | 38 (65% RH[(†)]) | Aerobic | $\approx 5$ ($\approx 0.5$) | (c) |
| CEM I (40%FA) | | | | | 11 (3) | |
| CEM I (40%LL) | | | | | 7 (1) | |

[(#)] Values in parenthesis correspond to unirradiated conditions.
[(*)] Values digitized from Fig. 6 in (Smart, Rance, and Werme 2008).
[(**)] Values digitized from Fig. 7 in (Smart, Rance, and Werme 2008).
[(†)] Curing RH before sealing the irradiation capsule. 1% $CO_2$ content.
[(a)] (Smart, Rance, and Werme 2008)
[(b)] (Dewynter-Marty et al. 2017)
[(c)] (Dabrowski et al. 2022)

### 3.2.2 Knowledge Gaps

The fundamental mechanism of gamma irradiation–induced corrosion carbon steel embedded in a cementitious matrix is not fully elucidated to date in order to draw conclusions about its significance for in-service irradiated concrete in LWRs. The hypothetical mechanism is a combination of a decrease of pH possibly caused by (1) gamma irradiation-induced carbonation and (2) the formation of radiolytic species. Two situations should be considered, depending on the presence or absence of a metal liner at the surface of the CBS. When the surface of the CBS is not protected by a metal liner, the irradiated concrete is subject to radiation-enhanced drying and $CO_2$ ingress. Gamma irradiation-induced carbonation has been reported by Vodák et al. (2005), Vodák et al. (2011), and Dabrowski et al. (2022). Calcite precipitation and pore distribution change were observed, although their effect on the strength of concrete is marginal (a few percent at about 1 MGy (Vodák et al. 2005)). However, it is hypothesized that pH may decrease to a unknown degree, thus causing acceleration of the corrosion current. It is unclear whether **the gamma dose rate affecting the formation of radiolytic gas and accelerated drying impacts the corrosion rate**. Dabrowski et al. (2022)'s electrochemical measurements could only be conducted after the gamma irradiation experiment. It is suspected that the corrosion rate may be correlated to the radiolytic gas production which decreases over time (Smart, Rance, and Werme 2008).

When the CBS includes a metal liner, concrete moisture remains trapped unless radiolytic gas diffusion through the pore network occurs. This condition is close but not equivalent to that of a fully saturated system. In this case, $CO_2$ ingress is not possible. However, corrosion rate increase has been observed in steel embedded in alkaline solution (Smart, Rance, and Werme 2008).

In addition, the **role of temperature on radiolytic reactions and corrosion kinetics** requires attention. Risner, Alpan, and Yang (2020) conducted hybrid radiation transport simulation of a 3-loop Westinghouse

PWR model and found that the irradiation-induced heating rate of embedded reinforcement bar near the reactor cavity is approximately 6 to 8 times higher than in the surrounding concrete.

Finally, irradiation-assisted stress-corrosion cracking (IASCC)—which causes intergranular stress corrosion cracking that occurs in irradiated austenitic alloys in nuclear environments—has been the subject of extensive research. However, this phenomenon is observed at fast neutron flux much higher than those expected in the embedded carbon-steel reinforcement. The **role of fast neutron irradiation on the formation of defects in the passivation layer products such as magnetite and the pristine low carbon steel** needs to be studied. Magnetite, hematite and iron spinel exhibit limited RIVE under $\sim 0.3\%$ at a fluence lower than $10^{20}$ n.cm$^{-2}$ at $E > 0.1$ MeV (Denisov, Dubrovskii, and Solovyov 2012) and $T < 80$ °C. The coefficient of thermal expansion of irradiated hematite does not appear to change (Dubrovskii et al. 1970). Post-neutron irradiation[11] electrical resistivity of magnetite increases by 50% (Shchennikov et al. 2009). The observed changes of properties under neutron irradiation indicate the formation of point defects and crystalline network distortion that may be susceptible to localized corrosion.

Table 4 provides a comparison between the gamma irradiation condition in PWR (Remec 2015) and experiments studying the effects of irradiation of the corrosion of steel embedded in cementitious matrix (Dewynter-Marty et al. 2017; Dabrowski et al. 2022) or alkaline solution (Smart, Rance, and Werme 2008).

Recommendations for future experiments are as follows:

- Temperature should be approximately 50 ± 10 °C.
- Two sets of RH conditions should be considered: (a) close to 100% RH to replicate conditions behind a liner, and (b) dry conditions of approximately 40% to model the operating conditions in an unlined CBS.
- The gamma dose rate and gamma dose cannot be simultaneously replicated in accelerated conditions. Experimental conditions are determined by the gamma source.

**Table 4. Comparison of gamma irradiation conditions in PWR and irradiation-induced corrosion experiment results published in the literature.**

| | PWR | (a) | (b) | (c) |
|---|---|---|---|---|
| Temperature (°C) | 40–65 | 30, 50 | 25 | 38 |
| RH (-) | $\lesssim$ 100%(*)<br>40-80%(**) | solution | 80% | 65% |
| $CO_2$ content (-) | 0.04%(***) | - | 0.04%? | 1% |
| Gamma dose rate (Gy h$^{-1}$) | 68-136 | 11, 300 | 15 | 300 |
| Gamma dose (kGy) | 60,000–120,000(d) | 1.8 | 130 | 1,800 |

(a) (Smart, Rance, and Werme 2008)
(b) (Dewynter-Marty et al. 2017)
(c) (Dabrowski et al. 2022)
(d) (Remec 2015) at 100 years of operation (92% load factor).
(*) High moisture content is expected when a liner is present.
(**) RH range from monitored humidity sensors embedded in concrete structures adjacent to the biological shield walls at Ringhals Unit 4 and Forsmark Unit 3 operated by Vatttenfall (Oxfall 2016).
(***) Atmospheric content.

11. $\Phi = 2.2 \times 10^{20}$ n.cm$^{-2}$.

## 4. CONCLUSIONS

The main conclusions of this literature review regarding the effects of irradiation and its synergistic effects with ASR and corrosion are as follows:

**Irradiation:** The knowledge gaps are clearly identified. The main gap is associated with the lack of understanding of the effects of fast neutron flux rate on concrete aggregate degradation. Preliminary data obtained from post-irradiation examination of aggregate specimens placed in test reactors provide evidence of a defect-healing mechanism governed by irradiation temperature. A thorough understanding of the exact nature of this healing mechanism remains to be established in order to extrapolate accelerated irradiation data to operational conditions in LWRSs. The collection and characterization of in-service irradiated concrete specimens is critical to making significant progress in this area. The second knowledge gap is associated with the neutron irradiation-induced relaxation of stresses in the concrete's cement paste, which was documented by a single publication from the early 1970s. Although arguments can be made regarding the origin of such a mechanism, further experimental evidence is needed. Both of the mentioned mechanisms are expected to be highly beneficial to the long-term operation of LWRs.

**IAASR:** This topic appears to be relevant only for CBSs that include a metallic liner on the surface of the concrete facing the reactor cavity and maintain a high moisture content in the irradiated concrete. The first stage of the mechanism involving the irradiation-enhanced dissolution of aggregate-forming minerals has been documented by researchers in Japan, Europe, and the United States, including institutions sponsored by DOE's NEUP. The subsequent reactive stages that cause the formation of expansive gel, leading to concrete damage, are poorly understood when occurring under irradiation conditions. This topic requires active research, including the design and completion of irradiation experiments to elucidate the possible mechanisms involved when irradiation and ASR are combined.

**IAC:** Literature on this topic is very limited. This coupled mechanism may include different modalities, causing aerobic corrosion of the reinforcement and other embedded anchors in unlined CBSs or anaerobic corrosion in lined CBSs. Aerobic corrosion appears to be associated with irradiation-induced carbonation of the concrete cover. Several knowledge gaps were identified: (1) the role of the gamma ray dose rate on the formation of radiolytic gas and the possible acceleration of drying, which impacts the corrosion rate; (2) the role of temperature on corrosion kinetics during irradiation; and (3) the role of fast neutrons in the formation of defects in the passivated oxide layer protecting the reinforcement. Novel irradiation experiments should be designed to address these gaps.

## 5. REFERENCES


Abd-Elssamd, A., Z.J. Ma, H. Hou, and Y. Le Pape. 2020. "Influence of mineralogical and chemical compositions on alkali-silica reaction of Tennessee limestones." *Construction and Building Materials* 261:119916. https://doi.org/10.1016/j.conbuildmat.2020.119916.

Abd-Elssamd, A., Z.J. Ma, Y. Le Pape, N.W. Hayes, and M. Guimaraes. 2020. "Effect of Alkali-Silica Reaction Expansion Rate and Confinement on Concrete Degradation." *ACI Materials Journal* 117, no. 1 (January). https://doi.org/10.14359/51720294.

Abdukadyrova, I.Kh. 2004. "Radiation-Induced Phase Transition of Quartz." *Inorganic Materials* 40 (11): 1350–1354.

———. 2008. "Effect of Neutron Irradiation on the High-Frequency IR Spectra of Quartz Glass." *Inorganic Materials* 44 (10): 1097–1100.

Allard, T. 1994. "La kaolinite: un dosimètre des rayonnements naturels. Application autraçage de migrations anciennes de radioéléments dans la géosphère." PhD diss., Université Paris VII.

Allard, T., and G. Calas. 2009. "Radiation effects on clay mineral properties." *Applied Clay Science* 43 (2): 143–149. ISSN: 0169-1317.

Almusallam, A.A. 2001. "Effect of degree of corrosion on the properties of reinforcing steel bars." *Construction and Building Materials* 15:361–388.

Almusallam, A.A., A.S. AlGahtani, A.R. Aziz, and Rasheeduzzafar. 1996. "Effect of reinforcement corrosion on bond strength." *Construction and Building Materials* 10 (2): 123–129.

Andrade, M., C. andKeddam, X.R. Nóvoa, C. Pérez, C.M. Rangel, and H. Takenouti. 2001. "Electrochemical behaviour of steel rebars in concrete: influence of environmental factors and cement chemistry." *Electrochimica Acta* 46:3905–3912.

Andreev, V.I., and D.A. Kapliy. 2014. "Stress-State of a Thick-Walled Cylindrical Shell under the Combined Action of Radiation and Temperature Field." *Advanced Materials Research* 1006-1007:177–180.

Apostolopoulos, C.A., S. Demis, and V.G. Papadakis. 2013. "Chloride-induced corrosion of steel reinforcement – Mechanical performance and pit depth analysis." *Construction and Building Materials* 38:139–146.

Bažant, Z.P., J.-C. Chern, and W. Thonguthai. 1982. "Finite element program for moisture and heat transfer in heated concrete." *Nuclear Engineering and Design* 68 (1): 61–70.

Bažant, Z.P., and M. Jirásek. 2018. *Creep and Hygrothermal Effects in Concrete Structures.* Vol. 225. Solid Mechanics and Its Applications. Springer.

Beltzung, F., and F.H. Wittmann. 2005. "Role of disjoining pressure in cement based materials." *Cement and Concrete Research* 35 (12): 2364–2370.

Bhargava, K., A.K. Ghosh, Y. Mori, and S. Ramanujam. 2007. "Corrosion-induced bond strength degradation of reinforced concrete - Analytical and empirical models." *Nuclear Engineering and Design* 237:1140–57.

Bibler, N.E., and E.G. Orebaugh. 1977. *Radiolytic gas production from tritiated waste forms – Gamma and alpha radiolysis studies.* Technical report DP-1459. Savannah River Laboratory.

Blosser, T.V., R.C. Reid, G.W. Bond, A.B. Reynolds, L.A. Lee, T.O. Speidel, D.T. Morgan, D.W. Vroom, J.F. Nichols, and M.A. Welt. 1958. *A Study of the Nuclear and Physical Properties of the ORNL Graphite Reactor Shield.* Technical report ORNL-2195. Oak Ridge National Laboratory, September.

Bolse, Wolfgang. 1998. "Formation and development of disordered networks in Si-based ceramics under ion bombardment." *Nuclear Instruments and Methods in Physics Research Section B: Beam Interactions with Materials and Atoms* 141 (1-4): 133–139.

Bouissonié, A., Z. Chen, Z. Qi, M. Collin, S.J. Zinckle, Y. Le Pape, E. Tajuelo Rodriguez, M. Bauchy, and G. Sant. 2025. "Radiation damages the silicates present in polyphasic mineral aggregates causing concrete's degradation." In preparation, *npj Materials Degradation.*

Bouniol, P. 2004. *State of knowledge on the water radiolysis in cemented waste forms and its approach by simulation.* Technical report CEA-R-6069. In French. CEA / Saclay 91191 Gif-sur-Yvette Cedex France: Commissariat à l'Energie Atomique.

———. 2010. "The influence of iron on water radiolysis in cement-based materials." *Journal of Nuclear Materials* 403, nos. 1-3 (August): 167–183.

Bouniol, P., and A. Aspart. 1998. "Disappearance of oxygen in concrete under irradiation: the role of peroxides in radiolysis." *Cement and Concrete Research* 28 (11): 1669–1681. ISSN: 0008-8846.

Bruck, P.M., T.C. Esselman, B.M. Elaidi, J.J. Wall, and E.L. Wong. 2019. "Structural assessment of radiation damage in light water power reactor concrete biological shield walls." *Nuclear Engineering and Design* 350:9–20.

Bykov, V.N., A.V. Denisov, V.B. Dubrovskii, V.V. Korenevskii, G.K. Krivokoneva, and L.P. Muzalevskii. 1981. "Effect of Irradiation Temperature on the Radiation Expansion of Quartz." *Atomnaya Energiya* 51 (3): 593–595.

Cabrera, J.G. 1996. "Deterioration of concrete due to reinforcement steel corrosion." *Cement and Concrete Composites* 18 (1): 47–59. https://doi.org/https://doi.org/10.1016/0958-9465(95)00043-7. https://www.sciencedirect.com/science/article/pii/0958946595000437.

Campbell, A.A. 2018. "Historical experiment to measure irradiation-induced creep of graphite." *Carbon* 139:279–288. ISSN: 0008-6223. https://doi.org/https://doi.org/10.1016/j.carbon.2018.06.055. https://www.sciencedirect.com/science/article/pii/S0008622318306213.

Cheniour, A., E. Davidson, Y. Le Pape, T. Pandya, B. Collins, B. Spencer, A. Godfrey, and M. Asgari. 2023. "A structural model of the long-term degradation of the concrete biological shield." *Nuclear Engineering and Design* 405:112217. ISSN: 0029-5493. https://doi.org/https://doi.org/10.1016/j.nucengdes.2023.112217. https://www.sciencedirect.com/science/article/pii/S0029549323000663.

Clark, R.G. 1958. *Radiation Damage to Concrete.* Technical report HW-56195. Hanford Laboratories, Richland WA: General Electric, March.

Craeye, B., G. De Schutter, C. Vuye, and I. Gerardy. 2015. "Cement-waste interactions: Hardening self-compacting mortar exposed to gamma radiation." *Progress in Nuclear Energy* 83:212–219.

Dabrowski, M., M.A. Glinicki, J. Kuziak, D. Jóźwiak-Niedźwiedzka, and K. Dziedzic. 2022. "Effects of 2 MGy gamma irradiation on the steel corrosion in cement-based composites." *Construction and Building Materials* 342:127967. ISSN: 0950-0618. https://doi.org/https://doi.org/10.1016/j.conbuildmat.2022.127967. https://www.sciencedirect.com/science/article/pii/S0950061822016373.

Denisov, A.V., V.B. Dubrovskii, and V.N. Solovyov. 2012. *Radiation Resistance of Mineral and Polymer Construction Materials.* In Russian. ZAO MEI Publishing House.

Dewynter-Marty, V., L. Chomat, W. Guillot, E. Amblard, D. Durand, M Cornaton, and X. Bourbon. 2017. "Concrete radiolysis effect on steels corrosion and comparison with non-irradiated material." In *EUROCORR 20th International Corrosion Congress/Process Safety Congress.* Prague, Czech Republic.

Donnan, F.G. 1911. "Theorie der Membrangleichgewichteund Membranpotentiale bei Vorhandensein von nichtdialysierenden Elektrolyten. Ein Beitrag zur physikalischchemischen Physiologie." *Z Elektrochem Angew PhysChem* 17:572–581.

Dubrovskii, V.B., S.S. IIbragimov, V.V. Korenevskii, A. Y. Ladygyn, V.K. Pergamenshchik, and V.S. Perevalov. 1970. "Hematite concrete for shielding against high neutron fluxes." *Atomnaya Energiya* 28 (3): 258–260.

Eby, R.K., R.C. Ewing, and R.C. Birtcher. 1992. "The amorphization of complex silicates by ion-beam irradiation." *Journal of Materials Research* 7 (11): 3080–3102.

Elleuch, L.F., F. Dubois, and J. Rappenau. 1971. "Behavior of Special Shielding Concretes and of their Constituents under Neutron Irradiation." In *Fourth United Nations International Conference on the Peaceful Uses of Atomic Energy,* 7.

Elleuch, L.F., F. Dubois, and J. Rappeneau. 1972. "Effects of Neutron Radiation on Special Concretes and Their Components." *Special Publication of The American Concrete Institute* 43:1071–1108.

Esselman, T., and P. Bruck. 2013. *Expected condition of concrete at age 80 of reactor operation.* Technical report A13276-R-001. 36 Main Street, Amesbury, MA 01913: Lucius Pitkins, Inc., September.

Ewing, R., B.C. Chakoumakos, G.R. Lumpkin, T. Murakami, R.B. Greegor, and F.W. Lytle. 1988. "Metamict minerals: Natural analogues for radiation damage effects in ceramic nuclear waste forms." *Nuclear Instruments & Methods in Physics Research* 32:487–497.

Ewing, R.C., B.C. Chakoumakos, G.R. Lumpkin, and T. Murakami. 1987. "The metamict state." *Materials Research Society Bulletin* 12:58–66.

Fernandez, I., J.M. Bairán, and A.R. Marí. 2015. "Corrosion effects on the mechanical properties of reinforcing steel bars. Fatigue and *sigma* – $\varepsilon$ behavior." *Construction and Building Materials* 101:772–783.

Field, K.G., I. Remec, and Y. Le Pape. 2015. "Radiation Effects on Concrete for Nuclear Power Plants – Part I: Quantification of Radiation Exposure and Radiation Effects." *Nuclear Engineering and Design* 282:126–143.

François, R., I. Khan, and V.H. Dang. 2013. "Impact of corrosion on mechanical properties of steel embedded in 27-year-old corroded reinforced concrete beams." *Materials and Structures* 46:899–910. https://doi.org/10.1617/s11527-012-9941-z.

Gholizadeh-Vayghan, A., and F. Rajabipour. 2017. "Quantifying the swelling properties of alkali-silica reaction (ASR) gels as a function of their composition." *Journal of the American Ceramic Society* 100 (8): 3801–3818. https://doi.org/https://doi.org/10.1111/jace.14893. eprint: https://ceramics.onlinelibrary.wiley.com/doi/pdf/10.1111/jace.14893. https://ceramics.onlinelibrary.wiley.com/doi/abs/10.1111/jace.14893.

Gholizadeh-Vayghan, F., A. anf Rajabipour. 2017. "The influence of alkali-silica reaction (ASR) gel composition on its hydrophilic properties and free swelling in contact with water vapor." *Cement and Concrete Research* 94:49–58.

Giebson, C., and K Seyfarth. 2025. "The colloidal nature and osmotic potential of alkali-silica reaction products and their role for the ASR expansion mechanism." *Materials and Structures* 58 (14). https://doi.org/10.1617/s11527-024-02542-4.

Giorla, A., Y. Le Pape, and H. Huang. 2016. "Meso-scale modeling of irradiation in pressurized water reactor concrete biological shield." In *Proceedings of FraMCoS-9,* edited by V. Saouma, J. Bolander, and E. Landis. Berkeley, CA: IA-FraMCoS, May. https://doi.org/10.21012/FC9.238. http://www.framcos.org/FraMCoS-9.php#gsc.tab=0.

Glasser, F.P. 1992. "Chemistry of the alkali-aggregate reaction." In *The Alkali Silica Reaction in Concrete,* edited by R.N. Swamy. Glasgow, UK: Blackie / Son Ltd.

Gournis, D., A. E. Mantaka-Marketou, M. A. Karakassides, and D. Petridis. 2000. "Effect of $\gamma$-irradiation on clays and organoclays: a Mössbauer and XRD study" [in English]. *Physics and Chemistry of Minerals* 27 (7): 514–521. ISSN: 0342-1791.

———. 2001. "Ionizing radiation-induced defects in smectite clays." *Physics and Chemistry of Minerals* 28:285–290.

Graves, H., Y. Le Pape, D. Naus, J. Rashid, V. Saouma, A. Sheikh, and J. Wall. 2014. *Expanded Material Degradation Assessment (EMDA), Volume 4: Aging of Concrete.* Technical report NUREG/CR-7153, ORNL/TM-2011/545. U.S. Nuclear Regulatory Commission.

Gray, B.S. 1971. "The effects of reactor radiation on cement and concrete." In *Proceedings of an Information Exchange Meeting on 'Results of Concrete Irradiation Programmes',* vol. EUR 4751 f-e. Brussels, Belgium: Commission des Communautés Européennes, April.

Guthrie, G.D., and J.W. Carey. 2015. "A thermodynamic and kinetic model for paste-aggregate interactions and the alkali-silica reaction." *Cement and Concrete Research* 76:107–120. ISSN: 0008-8846. https://doi.org/https://doi.org/10.1016/j.cemconres.2015.05.004. https://www.sciencedirect.com/science/article/pii/S0008884615001271.

Hansson, C.M. 1984. "Comments on electrochemical measurements of the rate of corrosion of steel in concrete." *Cement and Concrete Research* 14:574–584.

Hansson, C.M., A. Poursaee, and S.J. Jaffer. 2012. "Corrosion of Reinforcing Bars in Concrete." *The Masterbuilder,* no. PCA R&D Serial No. 31013, 106–124.

Harbsmeier, F., and W. Boise. 1998. "Ion beam induced amorphization in alpha quartz." *Journal of Applied Physics* 83 (8): 4049–4054.

Hartt, W. L., S. K. Lee, and E. Costa. 1997. "Condition Assessment and DeteriorationRate for Chloride Contaminated Reinforced Concrete Structures." In *International Seminar on Repair and Rehabilitation of RC Structures: the State of the Art.*

Hayes, N.W., W. Giorla A.B. anf Trent, D. Cong, Y. Le Pape, and Z.J. Ma. 2020. "Effect of alkali-silica reaction on the fracture properties of confined concrete." *Construction and Building Materials* 238 (117641): 13.

Hayes, N.W., C. Gui, A. Abd-Elssamd, Y. Le Pape, A.B. Giorla, S. Le Pape, E.R. Giannini, and Z.J. Ma. 2018. "Monitoring Alkali-Silica Reaction Significance in Nuclear Concrete Structural Members." *Journal of Advanced Concrete Technology* 16 (4): 179–190.

Helmuth, R.., D. Stark, S. Diamond, and M. Morenville-Régourd. 1993. *Silica Reactivity: An Overview of Research.* Technical report. National Research Council, Washington, DC: Highway Research Program.

Hickman, B.S., and W. Pryor. 1964. “The effects of neutron irradiation on beryllium oxide.” *Journal of Nuclear Materials* 14:96–110.

Hobbs, L., and M. Pascucci. 1980. “Radiolysis and defect structure in electron-irradiated $\alpha$-quartz.” *Journal de Physique Colloques* 41 (C6): 237–242.

Hsiao, Y.-H., E. Callagon La Plante, N.M.A. Krishnan, H.A. Dobbs, Y. Le Pape, N. Neithalath, M. Bauchy, J. Israelachvili, and G. Sant. 2018. “Role of the electrical surface potential and irradiation induced disordering on almandine’s dissolution kinetics.” Submitted, *The Journal of Physical Chemistry C* 122 (30): 17268–17277.

Hsiao, Y.-H., E. La Plante, N.M.A. Krishnan, Y. Le Pape, N. Neithalath, M. Bauchy, and G. Sant. 2017. “Effects of Irradiation on Albite’s Chemical Durability.” Submitted, *The Journal of Physical Chemistry A* 121:7835–7845.

Ichikawa, T., and T. Kimura. 2007. “Effect of Nuclear Radiation on Alkali-Silica Reaction of Concrete.” *Journal of Nuclear Science and Technology* 44 (10): 1281–1284.

Ichikawa, T., and H. Koizumi. 2002. “Possibility of radiation-induced degradation of concrete by alkali-silica reaction of aggregates.” *Journal of Nuclear Science and Technology (Tokyo, Japan)* 39:880–884.

Ichikawa, T., and M. Miura. 2007. “Modified model of alkali silica reaction.” *Cement and Concrete Research* 37:1291–97.

Imai, H., K. Arai, J. Isoya, H. Hosono, Y. Abe, and H. Imagawa. 1993. “Centers and oxygen hole centers in synthetic silica glasses by $\gamma$ irradiation.” *Physical Review B* 48 (3116): 3316–3123.

Inui, H., H. Mori, T. Sakata, and H. Fujita. 1990. “Electron irradiation induced crystalline-to-amorphous transition in quartz single crystals.” *Journal of Non-Crystalline Solids* 116:1–15.

Jennings, Hamlin M., Jeffrey J. Thomas, Julia S. Gevrenov, Georgios Constantinides, and Franz-Josef Ulm. 2007. “A multi-technique investigation of the nanoporosity of cement paste.” *Cement and Concrete Research* 37 (3): 329–336. ISSN: 0008-8846.

Jensen, V. 2004. “Alkali-silica reaction damage to Elgeseter Bridge, Trondheim, Norway: a review of construction, research and repair up to 2003.” EMABM 2003: 9th Euroseminar on Microscopy Applied to Building Materials, *Materials Characterization* 53 (2): 155–170. ISSN: 1044-5803. https://doi.org/https://doi.org/10.1016/j.matchar.2004.09.006. https://www.sciencedirect.com/science/article/pii/S1044580304002086.

Jóźwiak-Niedźwiedzka, D., R. Jaskulski, and M. Glinicki. 2016. “Application of Image Analysis to Identify Quartz Grains in Heavy Aggregates Susceptible to ASR inRadiation Shielding Concrete.” *Materials* 9 (224): 14 p.

Kambayashi, D., S. Sasano H. Sawada, K. Suzuki, and I. Maruyama. 2020. “Numerical Analysis of a Concrete Biological Shielding Wall under Neutron Irradiation by 3D RBSM.” *Journal of Advanced Concrete Technology* 18:617–632.

Kaplan, M.F. 1983. *Nuclear radiation and the properties of concrete.* Technical report No. 35. University of Cape Town.

———. 1989. *Concrete radiation shielding: Nuclear physics, concrete properties, design and construction.* Longman Scientific / Technical. ISBN: 0-582-03773-5.

Katayama, T. 2014. "ASR Gels and Their Crystalline Phases in Concrete – Universal Products in Alkali-Silica, Alkali-Silicate and Alkali-Carbonate Reactions." In *14th International Conference on Alkali-Aggregate Reaction.* https://icaarconcrete.org/wp-content/uploads/2022/10/14ICAAR-KatayamaT-2.pdf.

Khmurovska, Y., P. Štemberk, T. Fekete, and T. Eurajoki. 2019. "Numerical analysis of VVER-440/213 concrete biological shield undernormal operation." *Nuclear Engineering and Design* 350:58–66.

Kontani, O., Y. Ichikawa, A. Ishizawa, M. Takizawa, and O. Sato. 2010. "Irradiation Effects on Concrete Structure." In *International Symposium on the Ageing Management and Maintenance of Nuclear Power Plants,* 173–182.

Kontani, O., S. Sawada, I. Maruyama, M. Takizawa, and O. Sato. 2013. "Evaluation of Irradiation Effects on Concrete Structure – Gamma Ray Irradiation Tests on Cement Paste." In *Proceedings of the ASME 2013 Power Conference POWER2013.* 98099. Boston, MA, USA, July.

Krishnan, A.N.P., Y. Le Pape, G. Sant, and M. Bauchy. 2018. "Effect of irradiation on silicate aggregates' density and stiffness." *Journal of Nuclear Materials* 512 (October 8, 2018): 126–136. https://doi.org/10.1016/j.nucmat.2018.10.009.

Krishnan, A.N.P., B. Wang, Y. Le Pape, G. Sant, and M. Bauchy. 2017. "Irradiation- vs. Vitrification-Induced Disordering: The Case of $\alpha$-Quartz and Glassy Silica." Accepted, *Journal of Chemical Physics* 146 (20): 1–9.

Krivokoneva, G.K. 1976. "Structural Changes in feldspars under Impact of Radiation." (In Russian), *Crystal Chemistry and Structural Features of Minerals* Leningrad, Nauka:75–79.

Krivokoneva, G.K., and G.A. Sidorenko. 1971. "The essence of the metamict transformation in pyrochlores." *Geochemistry International* 8:113–122.

Krüger, M.E., H. Hilbig, L. Stelzner, and A. Machner. 2024. "Effect of the chemical composition of synthetic alkali-silica gels on their structure, swelling behavior and water uptake." *Cement and Concrete Research* 184 (107596).

Kunitz, M. 1928. "Syneresis and Swelling of Gelatin" [in eng]. *The Journal of general physiology* (United States) 12 (2): 289–312. ISSN: 0022-1295.

Lagerblad, B. 2012. "Alkali release from silicate minerals and alkali-silica reaction in concrete." In *Proceedings of the 14th International Conference on Alkali-Aggregate Reaction in Concrete,* edited by T. Drimalas, J.H. Ideker, and B. Fournier. 052411-LAGE. Austin, Texas, USA.

Larive, C. 1997. "Apports combinés de l'expérimentation et de modélisation à compréhension de l'alcali-réaction et de ses effets mécaniques." In French. PhD diss., Laboratoire Central des Ponts et Chaussées.

Le Caër, S. 2011. "Water Radiolysis: Influence of Oxide Surfaces on $H_2$ Production under Ionizing Radiation." *Water* 3 (1): 235–253. ISSN: 2073-4441. https://doi.org/10.3390/w3010235. https://www.mdpi.com/2073-4441/3/1/235.

Le Caër, S., P. Rotureau, F. Brunet, T. Charpentier, G. Blain, J.P. Renault, and J.C. Mialocq. 2005. "Radiolysis of Confined Water: Hydrogen Production at a High Dose Rate." *ChemPhysChem* 6 (12): 2585–2596.

Le Pape, Y. 2015. "Structural Effects of Radiation-Induced Volumetric Expansion on Unreinforced Concrete Biological Shields." *Nuclear Engineering and Design* 295:534–548.

Le Pape, Y., M. Alnaggar, and A. Cheniour. 2023. *Assessment of the Effect of the Irradiation-Induced Degradation on the In-Service Structural Performance of the Concrete Biological Shields.* Technical report ORNL/SPR-2023/3031 – M3LW-23OR0403013. Oak Ridge National Laboratory.

Le Pape, Y., M.H.F. Alsaid, and A.B. Giorla. 2018. "Rock-forming minerals radiation-induced volumetric expansion – Revisiting the literature data." *Journal of Advanced Concrete Technology* 16:191–209. https://doi.org/10.3151/jact.16.191.

Le Pape, Y., S. Henderson, S. Zinkle, and I. Remec. 2024. *High-Resolution 3D Simulation of Irradi-ated Concrete: Considerations for FluxEffects.* Technical report ORNL/SPR-2024/3511, M3LW-24OR0403013. Oak Ridge National Laboratory.

Le Pape, Y., J. Sanahuja, and M.H.F. Alsaid. 2020. "Irradiation-Induced Damage in Concrete-Forming Aggregates – Revisiting Literature Data Through Micromechanics." *Materials and Structures* 53 (62): 35. https://doi.org/10.1617/s11527-020-014.

Le Pape, Y., E. Tajuelo Rodriguez, P. Bran Anleu, A. Brooks, L.M. Anovitz, A. Alpan, J. Sheets, M. Koehler, G. Rother, and T.M. Rosseel. 2022. *Assessment of San Onofre concrete susceptibility against irradiation damage.* Technical report RIL 2022-07. U.S. Nuclear Regulatory Commission.

Lee, H.S., F. Tomosawa, and T. Noguchi. 1996. "Durability of Building Materials and Components." Chap. Reinforcement Corrosion-Induced Cover Cracking and Its Time Prediction for Reinforced Concrete Structures, edited by C. Sjöström, vol. 7. E&FN Spon.

Leemann, A. 2022. "Alkali silica reaction– sequence, products and possible mechanisms of expansion." In *16th International Conference on Alkali-Aggregate Reaction.* Lisbon, Portugal.

———. 2025. "Discussion of the paper "Effect of the chemical composition of synthetic alkali-silica gels on their structure, swelling behavior and water uptake" by Miriam E. Krüger, Harald Hilbig, Ludwig Stelzner and Alisa Machner, Cem. Conc. Res. 184 (2024): 107596." *Cement and Concrete Research* 189 (107778).

Leemann, A., and B. Münch. 2019. "The addition of caesium to concrete with alkali-silica reaction: Implications on product identification and recognition of the reaction sequence" [in eng]. *Cement and concrete research* (Elmsford) 120:27–35. ISSN: 0008-8846.

Leemann, A., and T. Takayma. 2021. "Introduction to Diagnosis." In *Diagnosis & Prognosis of AAR Affected Structures, State-of-the-Art Report of the RILEM Technical Committee 259-ISR.*

Łowińska-Kluge, A., and P.e Piszora. 2008. "Effect of gamma irradiation on cement composite observed with XRD and SEM methods in the range of radiation dose 0–1409 MGy." *Acta Physica Polonica* 114 (2): 399–411.

Manzano-Santamaría, J., J. Olivares, A. Rivera, and F. Agulló-López. 2012. "Electronic damage in quartz (c-$SiO_2$) by MeV ion irradiations: Potentiality for optical waveguiding applications." Proceedings of the 17th International Conference on Ion Beam Modification of Materials (IBMM 2010), *Nuclear Instruments and Methods in Physics Research Section B: Beam Interactions with Materials and Atoms* 272:271–274. ISSN: 0168-583X.

Maruyama, I., S. Ishikawa, J. Yasukouchi, S. Sawada, R. Kurihara, M. Takizawa, and O. Kontani. 2018. "Impact of gamma-ray irradiation on hardened white Portland cement pastes exposed to atmosphere." *Cement and Concrete Research* 108:59–71.

Maruyama, I., O. Kontani, M. Takizawa, S. Sawada, S. Ishikawa, J. Yasukouchi, O. Sato, J. Etoh, and T. Igari. 2017. "Development of the Soundness Assessment Procedure for Concrete Members Affected by Neutron and Gamma-Irradiation." *Journal of Advanced Concrete Technology* 15:440–523.

Maruyama, I., A. Meawad, T. Kondo, S. Sawada, P. Halodova, A. Fedorikova, T. Ohkubo, et al. 2023. "Radiation-induced alteration of sandstone concrete aggregate." *Journal of Nuclear Materials* 583:154547. ISSN: 0022-3115. https://doi.org/https://doi.org/10.1016/j.jnucmat.2023.154547. https://www.sciencedirect.com/science/article/pii/S0022311523003148.

Maruyama, I., K. Murakami, T. Ohkubo, S. Sawada, O. Kontani, T. Igari, M. Kawai, and J. Etoh. 2025. "Neutron flux impact on rate of expansion of quartz." In press. *Journal of Nuclear Materials* 606 (155631).

Maruyama, I., Y. Nishioka, G. Igarashi, and K. Matsui. 2014. "Microstructural and bulk property changes in hardened cement paste during the first drying process." *Cement and Concrete Research* 58:20–34.

Mayer, G, and M Lecomte. 1960. "Effet des neutrons rapides sur le quartz cristallin et la silice vitreuse." *Le Journal de Physique et le Radium* 21 (12): 846–852.

Mayer, G., and J. Gigon. 1956. "Effets des neutrons rapides sur quelques constantes physiques du quartz cristallin et de la silice vitreuse." *Le Journal de Physique et le Radium* 18:109–114.

Mazars, J., and G. Pijaudier-Cabot. 1989. "Continuum Damage Theory –Application to Concrete." *Journal of Engineering Mechanics – ASCE* 115:345–365.

McDowall, D.C. 1971. "The Effects of Gamma Radiation on the Creep Properties of Concrete." In *Proceedings of an Information Exchange Meeting on 'Results of Concrete Irradiation Programmes',* vol. EUR 4751 f-e, 55–69. Brussels, Belgium: Commission des Communautés Européennes, April.

Miura, M., and T. Ichikawa. 1996. "The role of calcium ions in the formation of crack in concrete by alkali-silica reaction." *Kensetsuyou Genzairyou* 6:43–48.

Morinaga, S. 1990. "Prediction of Service Lives of Reinforced Concrete Buildings Based on the Corrosion Rate of Reinforcing Steel." In *Durability of Building Materials and Components.* E&FN Spon, London, England.

Myers, R.J., S.A. Bernal, R. San Nicolas, and J.L. Provis. 2013. "Generalized Structural Description of Calcium-Sodium Aluminosilicate Hydrate Gels: The Cross-Linked Substituted Tobermorite Model." *Langmuir* 29:5294–5306.

Naus, D.J. 2009. *Inspection of Nuclear power Plant Structures - Overview of Methods and Related Applications.* Technical report ORNL/TM-2007/191. Oak Ridge National Laboratory, May.

Ouglova, A., M.L.M. François, Y. Berthaud, S. Caré', and F. Foct. 2006. "Mechanical properties of an iron oxide formed by corrosion in reinforced concrete structures." *Journal de Physique IV Proceedings* 136:99–107. ISSN: 1155-4339.

Oxfall, M. 2016. "Climatic conditions inside nuclear reactors containments. Evaluation of moisture condition in the concrete within reactor containments and interaction with ambient compartments." Report TVBM-1035. PhD diss., Lund University.

Petti, J.P., D.J. Naus, A. Sagüés, R.E. Weyers, B.A. Erler, and N.S. Berke. 2011. *Nuclear containment steel liner corrosion workshop: final summary and recommendation report.* Technical report SAND2010-8717. Sandia National Laboratory, July.

Pfeffer, R.L. 1985. "Damage center formation in $SiO_2$ thin films by fast electron irradiation." *Journal of Applied Physics* 57:5176–5180.

Pignatelli, I., A. Kumar, R. Alizadeh, Y. Le Pape, M. Bauchy, and G. Sant. 2016. "A dissolution-precipitation mechanism explains the origin of concrete creep in moist environments." *J. Chem. Phys.* 145:054701.

Pignatelli, I., A. Kumar, K.G. Field, B. Wang, Y. Yu, Y. Le Pape, M. Bauchy, and G. Sant. 2016. "Direct Experimental Evidence for Differing Reactivity Alterations of Minerals following Irradiation: The Case of Calcite and Quartz." Accepted for publication, *Scientific Reports – Nature* 6(20155):1–10. https://doi.org/10.1038/srep20155.

Pomaro, B., V.A. Salomoni, F. Gramegna, G. Prete, and C.E. Majorana. 2011. "Radiation damage evaluation on concrete within a facility for Selective Production of Exotic Species (SPES Project), Italy." *Journal of Hazardous Materials* 194 (0): 169–177. ISSN: 0304-3894.

Poole, A. B., and I. Sims. 2017. *Alkali-aggregate reaction in concrete: a world review* [in eng]. 1st ed. Boca Raton, FL: CRC Press. ISBN: 1-317-48442-8.

Potts, A., and L. Leay. 2021. "Evidence for pore water composition controlling carbonate morphology in concrete and the further effect of gamma radiation." *Construction and Building Materials* 275:122049. ISSN: 0950-0618. https://doi.org/https://doi.org/10.1016/j.conbuildmat.2020.122049. https://www.sciencedirect.com/science/article/pii/S0950061820340526.

Pourbaix, M. 1966. *Atlas of Electrochemical Equilibria in Aqueous Solutions.* 307. Pergamon Press.

Poursaee, A., and C.M. Hansson. 2007. "Reinforcing steel passivation in mortar and pore solution." *Cement and Concrete research* 37:1127–1133.

Primak, W. 1958. "Fast-Neutron-Induced Changes in Quartz and Vitreous Silica" [in English]. *Physical Review* (One Physics Ellipse, College PK, MD 20740-3844 USA) 110 (6): 1240–1254. ISSN: 0031-899X.

———. 1976. "Extrusion of quartz on ion bombardment: Further evidence for radiation-induced stress relaxation of the silica network" [in English]. *Physical Review B* (One Physics Ellipse, College Pk, MD 20740-3844 USA) 14 (10): 4679–4686. ISSN: 0163-1829.

Rajabipour, F., E. Giannini, C. Dunant, J. H. Ideker, and M. D. Thomas. 2015. "Alkali-silica reaction: current understanding of the reaction mechanisms and the knowledge gaps." *Cement and Concrete Research* 76:130–146.

Remec, I. 2013. "Radiation Environment in Concrete Biological Shields of Nuclear Power Plants." Light Water Reactor Sustainability Program.

———. 2015. *Status Report on Defining a Unified Parameter for Characterization of Radiation Intended for Evaluation of Radiation-Induced Degradation of Concrete.* Technical report ORNL/LTR-2015/542. Oak Ridge National Laboratory, September.

Remec, I., T.M. Rosseel, K.G. Field, and Y. Le Pape. 2018. "Radiation-Induced Degradation of Concrete in NPPs." In *Reactor Dosimetry: 16th International Symposium,* edited by M.H. Sparks, K.R. DePriest, and D.W. Vehar, vol. ASTM STP1608, 201–211. https://doi.org/doi:10.1520/STP160820170059.

Risner, J., A. Alpan, and J. Yang. 2020. *Radiation Evaluation Methodology for Concrete Structures.* Technical report NUREG/CR-7281 ORNL/SPR-2020/1572. Oak Ridge: Oak Ridge National Laboratory.

Rotureau, P., J. P. Renault, B. Lebeau, J. Patarin, and J.-C. Mialocq. 2005. "Radiolysis of Confined Water: Molecular Hydrogen Formation." *ChemPhysChem* 6 (7): 1316–1323. ISSN: 1439-7641.

Rymeš, J., I. Maruyama, R. Shimamoto, A. Tachibana, Y. Tanaka, S. Sawada, Y. Ichikawa, and O. Kontani. 2019. "Long-term Material Properties of a Thick Concrete Wall Exposed to Ordinary Environmental Conditions in a Nuclear Reactor Building: the Contribution of Cement Hydrates and Feldspar Interaction." *Journal of Advanced Concrete Technology* 17 (5): 195–215. https://doi.org/10.3151/jact.17.195.

Sadek, F.H., T. Thonstad, S. Marcu, J. Weigand, T. Barrett, H. Lew, L. Phan, and A. Pintar. 2021. *Structural Performance of Nuclear Power Plant Concrete Structures Affected by Alkali-Silica Reaction (ASR) - Task 1: Assessing In-Situ Mechanical Properties of ASR-Affected Concrete* [in en], 2021-02-08 00:02:00. https://doi.org/https://doi.org/10.6028/NIST.TN.2121. https://tsapps.nist.gov/publication/get_pdf.cfm?pub_id=930667.

Saouma, V., and L. Perotti. 2006. "Constitutive Model for Alkali-Aggregate Reactions." *ACI Materials Journal* 103, no. 3 (May): 194–2002.

Seeberger, J., and H.K. Hilsdorf. 1982. *Einfluss von radioactiver Strahlung auf die Festogkeit and Struktur von Beton.* Technical report NR 2505. Institut fur Massivbau and Baustofftechnologie, Universitat Karlsruhe.

Shchennikov, V.V., S.V. Ovsyannikov, A.E. Karkin, S. Todo, and Y. Uwatoko. 2009. "Galvanomagnetic properties of fast neutron bombarded $Fe_3O_4$ magnetite: A case against charge ordering mechanism of the Verwey transition." *Solid State Communications* 149 (19): 759–762. ISSN: 0038-1098. https://doi.org/https://doi.org/10.1016/j.ssc.2009.03.002. https://www.sciencedirect.com/science/article/pii/S0038109809001252.

Silva, C.M., T.M. Rosseel, and M.C. Kirkegaard. 2018. "Radiation-Induced Changes in Quartz, A Mineral Analog of Nuclear Power Plant Concrete Aggregates." *Inorganic Chemistry* 57:3329–3338.

Smart, N.R., A.P. Rance, and L.O. Werme. 2008. "The effect of radiation on the anaerobic corrosion of steel." *Journal of Nuclear Materials* 379 (1): 97–104. https://doi.org/https://doi.org/10.1016/j.jnucmat.2008.06.007. https://www.sciencedirect.com/science/article/pii/S0022311508003310.

Stark, D. 1991. "The moisture condition of field concrete exhibiting alkali-silica reactivity." 2nd CANMET/ACI International Conference on Durability of Concrete, Montreal, *American Concrete Institute, ACI Special Publication* SP-126:973–987. ISSN: 01932527.

Struble, L.J., and S. Diamond. 1981. "Swelling Properties of Synthetic Alkali Silica Gels" [in eng]. *Journal of the American Ceramic Society* (Oxford, UK) 64 (11): 652–655. ISSN: 0002-7820.

Takatura, T., T. Ishikawa, N. Matsumoto, S. Mitsuki, K. Takiguchi, and Y. Masuda. 2005. "Investigation of the expanded value of turbine generator foundation affected by alkali-silica reaction." In *Proceedings of the 18th International Conference on Structural Mechanics in Reactor Technology (SMIRT18),* 2061–2068. SMIRT18-H03-7. Beijing, China.

Taylor, H. F. W., and D.E. Newbury. 1984. "Calcium hydroxide distribution and calcium silicate hydrate composition in tricalcium silicate and $\beta$-dicalcium silicate pastes." *Cement and Concrete Research* 14 (1): 93–98. ISSN: 0008-8846.

Thonstad, T, J. Weigand, F.H. Sadek, S. Marcu, T. Barrett, H. Lew, L. Phan, and A. Pintar. 2021. *Structural Performance of Nuclear Power Plant Concrete Structures Affected by Alkali-Silica Reaction (ASR) - Task 2: Assessing Bond and Anchorage of Reinforcing Bars in ASR-Affected Concrete* [in en], 2021-02-03 00:02:00. https://doi.org/https://doi.org/10.6028/NIST.TN.2127. https://tsapps.nist.gov/publication/get_pdf.cfm?pub_id=930666.

Uchikoshi, G., Y. Koshiro, and T. Koyama. 2024. "36-Year Monitoring of Full-Scale Mass Concrete Test Pieces at Nuclear Power Plant Part 1: Study of Physical Properties of Concrete Cast in Hot Weather Environment of Japan." In *27th International Conference on Structural Mechanics in Reactor Technology,* Division I. Yokohama, Japan.

Vodák, F., K. Trtik, V. Sopko, O. Kapičková, and P. Demo. 2005. "Effect of $\gamma$-irradiation on strength of concrete for nuclear-safety structures." *Cement and Concrete Research* 35 (7): 1447–1451.

Vodák, F., V. Vydra, K. Trtik, and O. Kapičková. 2011. "Effect of gamma irradiation on properties of hardened cement paste." *Materials and Structures* 44:101–107.

Weigand, J., F.H. Sadek, T. Thonstad, S. Marcu, R. Villegas, L. Phan, and A.L. Pintar. 2021. *Structural Performance of Nuclear Power Plant Concrete Structures Affected by Alkali-Silica Reaction (ASR). Task 3: Assessing Cyclic Performance of ASR-Affected Concrete Shear Walls* [in en], 2021-09-27 04:09:00. https://tsapps.nist.gov/publication/get_pdf.cfm?pub_id=932991.

White, S. 1977. "Geological significance of recovery and recrystallization processes in quartz." Fabrics, microstructures, and microtectonics, *Tectonophysics* 39 (1): 143–170. ISSN: 0040-1951. https://doi.org/https://doi.org/10.1016/0040-1951(77)90093-2. https://www.sciencedirect.com/science/article/pii/0040195177900932.

Wittels, M., and F.A. Sherrill. 1954. "Radiation damage in $SiO_2$ structures." *Physical Review* 93:1117–1118.

Xia, J., W. Jin, Y. Zhao, and L. Li. 2013. "Mechanical performance of corroded steel bars in concrete." *Structures and Buildings* 166 (SB5): 235–246.

Yano, T., K. Fukuda, M. Imai, and H. Miyazaki. 2007. "Physical property changes of crystalline and non-crystalline $SiO_2$ due to neutron irradiation and recovery by subsequent annealing." Proceedings of the Twelfth International Conference on Fusion Reactor Materials (ICFRM-12), *Journal of Nuclear Materials* 367-370:730–735.

Yokokura, K., O. Kontani, S. Sawada, and I. Maruyama. 2024. "Compressive Strength of Massive Concrete Structure Members Increasing from the Surface to the Inside." In *27th International Conference on Structural Mechanics in Reactor Technology,* Division I. Yokohama, Japan.

Ziegler, J.F. 1977-1985. *The Stopping and Range of Ions in Matter.* Vol. 2-6. Pergamon Press.

Zubov, V. 1956. "Variation of the elastic constants of quartz with temperature." *Doklady Akademii Nauk SSSR* 107:392–393.

Zubov, V.G., and A.T. Ivanov. 1966. "Expansion of quartz caused by irradiation with fast neutrons." *Soviet Physics Crystallography* 11 (3): 372–374.

———. 1967. "Elasticity of quartz irradiated with fast neutrons." *Soviet Physics Crystallography* 12, no. 2 (September): 313–314.

Zubov, V.G., and L.P. Osipova. 1971. "Raman study of radiative alpha-beta transition in quartz." *Soviet Physics Crystallography, USSR* 15 (5): 863–&. ISSN: 0038-5638.